Numerical upscaling of seismic signatures of poroelastic rocks containing mesoscopic fluid-saturated voids

Yanbin He[1, 2], J. Germán Rubino[3], Santiago G. Solazzi[2], Nicolás D. Barbosa[2], Marco Favino[2], Tianning Chen[1], Jinghuai Gao[4], Klaus Holliger[2]

[1]School of Mechanical Engineering, Xi'an Jiaotong University, Xi'an, China,

[2]Institute of Earth Sciences, University of Lausanne, Lausanne, Switzerland,

[3]CONICET, Centro Atómico Bariloche - CNEA, San Carlos de Bariloche, Argentina,

[4]School of Information and Communications Engineering, Xi'an Jiaotong University, Xi'an, China

Corresponding author: J. Germán Rubino (german.rubino@cab.cnea.gov.ar)

Key Points:

- We develop a numerical upscaling procedure to calculate seismic signatures based on a novel coupled fluid-poroelastic model.
- In the presence of fluid-saturated mesoscopic voids, the newly proposed coupled approach is more flexible and more accurate than existing methodologies.
- Application to a synthetic "vuggy" carbonate-type rock sample provides new insights into seismic energy dissipation related to fluid pressure diffusion between micro- and meso-scale pores.

This article has been accepted for publication and undergone full peer review but has not been through the copyediting, typesetting, pagination and proofreading process, which may lead to differences between this version and the Version of Record. Please cite this article as doi: 10.1029/2021JB023473.

Abstract

We present a novel coupled fluid-poroelastic model and an associated numerical upscaling procedure to calculate seismic attenuation and velocity dispersion in porous rocks induced by fluid pressure diffusion (FPD) in the presence of mesoscopic fluid-saturated voids, such as, for example, vugs or factures. By applying appropriate interface conditions, the proposed model couples the Navier-Stokes equations for viscous fluids with Biot's equations of poroelasticity to model the mesoscopic voids and the embedding background, respectively. A finite element method is employed to solve the coupled problem for a set of three relaxation tests, which enables us to compute the complex-valued and frequency-dependent equivalent stiffness matrix of the considered synthetic sample. The newly proposed fluid-poroelastic approach is compared with a purely poroelastic one as well as a fluid-elastic approach in a benchmark model containing interconnected mesoscopic fractures embedded in a poroelastic background. We obtain excellent agreement for the proposed approach and the purely poroelastic model by optimizing the material properties of the fractures for the latter, which demonstrates both the correctness and advantages of our method over the purely poroelastic approach for modeling fluid-saturated mesoscopic voids. We also observe that, while the coupled fluid-elastic approach and the proposed method provide consistent results with regard to seismic attenuation due to the fracture-to-fracture FPD, the latter also allows to account for the effects of fracture-to-background FPD. Finally, we employ the proposed methodology to explore the seismic characteristics of a synthetic "vuggy" carbonate-type sample, for which we visualize and interpret the resulting seismic attenuation in terms of FPD between the microscopic and mesoscopic pores.

Plain Language Summary

Seismic waves are commonly employed to study porous and/or fractured geological formations in the Earth's upper crust. In the presence of relatively small heterogeneities, such as fluid-saturated fractures or vugs, seismic waves may exhibit velocity variation and amplitude decay due to fluid pressure diffusion processes, which are important characteristics of seismic waves. To date, it remains difficult to understand how complex and fluid-saturated voids impact these seismic characteristics. To address this problem, we propose a novel coupled fluid-poroelastic model and develop a corresponding numerical upscaling procedure to calculate seismic characteristics of

porous media containing mesoscopic heterogeneities. Our results demonstrate that the proposed approach is more accurate and flexible than previous related models, which, in turn, opens new and interesting perspectives for the seismic exploration of corresponding geological environments.

1 Introduction

The remote detection and characterization of fluid-saturated features, such as, for example, fractures and vugs, is of preeminent importance in many scenarios of applied and environmental geophysics, including groundwater management and remediation, hydrocarbon exploration, and geothermal energy production (e.g., Klimentos, 1995; Jha et al., 2007; Tester et al., 2007). Seismic methods are widely recognized as being particularly effective and valuable in this regard (e.g., Liu & Martinez, 2012). However, for rocks containing fluid inclusions in the mesoscopic scale range, that is, larger than the typical pore and grain sizes but much smaller than the prevailing wavelengths, the seismic resolution is generally insufficient to allow for direct imaging of such features. Therefore, most related research efforts focus on analyses of particular attributes of seismic data. Notably, seismic attenuation and velocity dispersion as well as corresponding variations with the direction of wave propagation have been identified as diagnostic features that may permit to estimate valuable properties of heterogeneous porous rocks, such as, for example, fluid saturation, fracture orientations, and fracture compliances (e.g., Liu et al., 2007; Müller et al., 2010; Schijns et al., 2012).

In the presence of fluid-filled pores and/or voids, a passing seismic wave causes fluid pressure gradients and, thus, dissipates energy due to viscous friction. This mechanism of seismic attenuation is generally referred to as wave-induced fluid flow (WIFF) or fluid pressure diffusion (FPD). White (1975) first proposed this mechanism at the mesoscopic scale and Dutta & Ode (1979a, 1979b) subsequently framed it in the context of Biot's (1941, 1962) theory of poroelasticity. Pride et al. (2004) developed a double-porosity model to include the effect of mesoscopic fluid inclusions on the basis of Biot's (1941, 1962) theory. Ba et al. (2011) also presented the so-called Biot-Rayleigh theory for double-porosity media, which provides qualitatively similar seismic attenuation of fast compressional wave with that of Pride's model

(2004) but allows to calculate additionally the velocity and attenuation of two slow compressional waves. More recently, Fu et al. (2018, 2020) derived numerical solutions to quantify seismic dispersion and attenuation as well as semi-analytical solutions to assess frequency-dependent velocity anisotropy of porous rocks in the presence of a sparse distribution of aligned slit cracks. Due to inherent limitations of the above analytical solutions, accurate numerical schemes for calculating seismic signatures in porous rocks with mesoscopic- scale heterogeneities are needed, for example, for heterogeneities with complex geometries and/or spatial distributions. Although many numerical schemes have been developed to solve the poroelastic wave equations in heterogeneous media, they become computationally inefficient when used to calculate seismic attenuation due to WIFF. This is due to the fact that seismic wave propagation and wave-induced FPD prevail at significantly different spatial scales. Correspondingly, numerical upscaling techniques based on creep and/or relaxation tests are currently the most efficient approaches to quantify the corresponding FPD effects (Masson & Pride, 2007; Rubino et al., 2009; Wenzlau et al., 2010; Quintal et al., 2011).

Numerical upscaling approaches for assessing the seismic response of heterogeneous porous rocks are commonly based on Biot's (1941, 1962) equations, where mesoscopic heterogeneities are represented as poroelastic features with different hydraulic and mechanical properties compared to the embedding porous background (e.g., Brajanovski et al., 2005; Rubino et al., 2013, 2014). Masson and Pride (2007) proposed a quasi- static creep test to estimate seismic attenuation induced by FPD with a finite difference algorithm. Rubino et al. (2009) presented a related numerical upscaling procedure to calculate equivalent seismic signatures of heterogeneous fluid-saturated porous media based on a frequency-domain finite element method. Wenzlau et al. (2010) and Carcione et al. (2011) performed numerical relaxation experiments based on the poroelastic equations to estimate equivalent seismic characteristics in the presence of effective vertical transverse isotropy (VTI). Quintal et al. (2011) solved the so-called *u-p* form of Biot's (1941) consolidation equations to upscale seismic signatures of poroelastic rocks with mesoscopic heterogeneities. Masson and Pride (2014) extended their original isotropic methodology (Masson & Pride, 2007) to orthotropic materials. The common aspect shared by all these works is that they are designed for isotropic or specific anisotropic systems of relatively high symmetry. To overcome this limitation, Rubino et al. (2016) developed a fully generalized numerical upscaling

procedure that allows for computing equivalent seismic signatures in the presence of arbitrary effective anisotropy.

Although the Biot-based upscaling procedures mentioned above facilitate the study of the effects of FPD on seismic signatures (e.g., Rubino et al., 2013, 2014, 2017; Hunziker et al., 2018; Solazzi et al., 2020), they are only effective as long as the considered mesoscopic heterogeneities can be represented as porous features. However, in some scenarios, such as in the presence of vugs and open fractures, the mesoscopic heterogeneities effectively correspond to fluid-saturated voids, which, in turn, defies their representation as parts of a poroelastic continuum. While attempts have been made to model mesoscopic voids as fluid-saturated inclusions (e.g., Chapman, 2003, Hudson, 1981, Quintal, 2016, 2019), the common limitation of these approaches is that they do not allow for a comprehensive quantification of FPD effects. For example, corresponding analytical characterizations (e.g., Hudson, 1981; Chapman, 2003) assume simplified geometries of fluid inclusions and, hence, their applicability is restricted to idealized geometries and they cannot properly account for interactions between fluid inclusions (Lissa et al., 2019). On the other hand, current numerical approaches dealing with fluid-saturated voids (Quintal et al., 2016, 2019) cannot adequately describe the multiplicity of scales associated with FPD effects because the background is modeled as an elastic solid. Vinci et al. (2014b) studied seismic attenuation associated with flow in fractures based on a hybrid upscaling approach (Vinci et al., 2014a), where the background medium is characterized by Biot's (1941) quasi-static poroelastic equations, while the dynamic aspect related to fluid flow within the fractures is approximated by a 1D solution of the Navier-Stokes (NS) equations in the laminar regime. Due to the assumption of axial symmetry and the use of the cubic law for the approximation of the fluid flow in fractures, the applicability of this approach is, however, limited to idealized and simplistic scenarios. For example, it is neither applicable to fracture surfaces with asperities and/or contact areas nor to multiple intersecting fractures.

To overcome these limitations, we propose a novel upscaling framework, in which the mesoscopic fluid-saturated voids are represented by the linearized quasi-static NS equations (Landau & Lifshitz, 1959), while the embedding poroelastic background is described by the Biot's (1941)

consolidation equations. The two systems of equations are coupled using appropriate interface conditions. The numerical upscaling procedure is then implemented by solving the coupled problem with a finite element method for three oscillatory relaxation tests applied to a representative elementary volume (REV) of the heterogeneous formation of interest. The spatially averaged responses of the probed REV enable us to determine the components of an effective frequency-dependent and complex-valued symmetric stiffness matrix through a least-squares procedure (Rubino et al., 2016), which, in turn, permits to obtain the anisotropic seismic response of the formation of interest. An important advantage of the proposed approach is that, while being more flexible with respect to the representation of mesoscopic fluid-saturated voids than current methods, it also permits to quantify the associated FPD effects without the need to replace the fluid inclusions with equivalent media. Moreover, this novel methodology enables us to assess in which scenarios a purely poroelastic representation is appropriate for estimating seismic signatures of porous media containing mesoscopic fluid inclusions. We validate the proposed approach by first making a comprehensive comparison with pertinent benchmark models of fractured samples before considering a more realistic synthetic vuggy carbonate-type model, where we analyze the seismic attenuation due to fluid pressure communication between the prevailing mesoscopic and microscopic pores.

2 Methodology

Figure 1a illustrates the concept of seismic wave propagation in a heterogeneous porous environment, which locally may contain fluid filled voids, such as, for example, fractures, vuggy pores, and karstic dissolution features. To determine the dynamic properties of the probed porous medium, we consider REVs of the formations of interest (Figure 1b). Figure 1c illustrates a canonical example of a fluid inclusion Ω_f embedded in a poroelastic domain Ω_p. To model the response of the heterogeneous medium under harmonic deformation, we consider Biot's (1941) consolidation equations and the linearized NS equations (Landau & Lifshitz, 1959; Quintal et al., 2016) to describe the behavior of the poroelastic background and the fluid inclusion, respectively. The two domains are coupled by imposing suitable conditions along the interface Γ_{pf}. Several oscillatory relaxation tests are carried out under appropriate boundary conditions (BCs) along external edges of the REV. This enables us to calculate the harmonic response of the coupled system in term of, for example, the averaged stresses and strains, the fluid pressure distribution as

well as the local energy dissipation. Assuming that the probed poroelastic environment containing mesoscopic fluid inclusions can be approximated by a homogeneous anisotropic viscoelastic medium at the wavelength scale, we can estimate the complex-valued and frequency-dependent stiffness matrix of the equivalent viscoelastic medium using the averaged stresses and strains (Rubino et al., 2016). Finally, we solve the corresponding viscoelastic wave equations to calculate the effective phase velocities and inverse quality factors as functions of frequency and direction of propagation. In the following, we introduce the mathematical description of the proposed methodology.

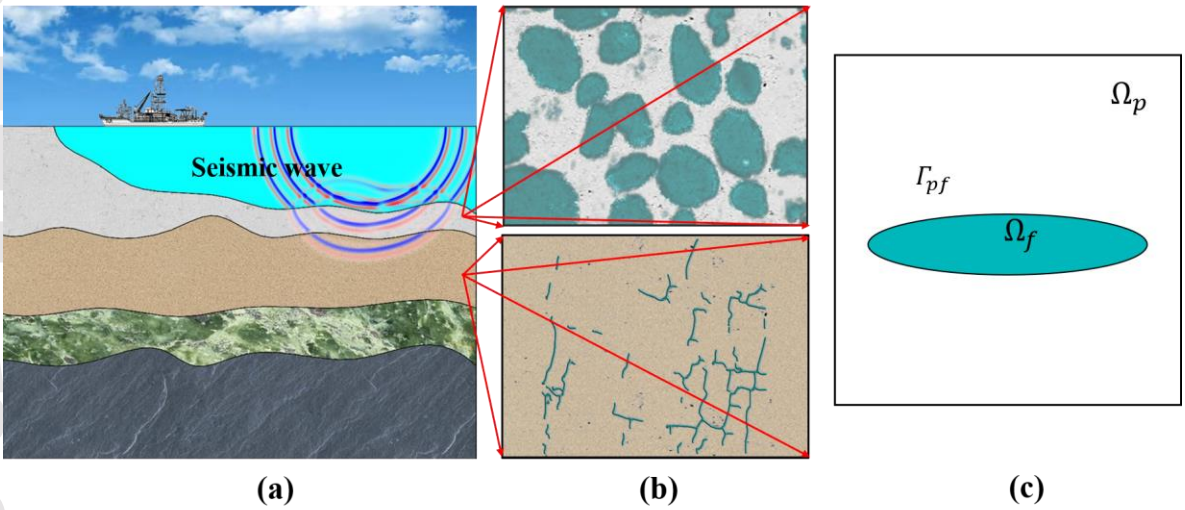

Figure 1. Schematic illustration of the problem considered in this study. (a) Seismic wave propagation in heterogeneous porous environment containing fluid-filled voids. (b) Conceptual representation of two typical types of such fluid inclusions (green color) embedded in a porous background (gray color). Top: carbonate-type vuggy mesopores (modified from Anselmetti et al., 1998); bottom: fracture network in a porous medium (modified from Montemagno & Pyrak-Nolte, 1995). (c) Sketch of fluid-filled void Ω_f embedded in a porous background Ω_p.

2.1 Coupled System of NS-Biot Equations

When a seismic wave propagates through porous rocks containing mesoscopic fluid inclusions, it experiences attenuation and velocity dispersion in response to energy dissipation. In the context of this work, the dominant physical process of interest is FPD and, hence, inertial effects can generally be neglected (Rubino et al., 2016). In the following, we outline a new model to adequately describe this phenomenon in the presence of mesoscopic fluid-filled voids, which uses

the Biot's (1941) consolidation equations to describe the porous background and the linearized quasi-static NS equations to characterize the fluid inclusions.

In the poroelastic domain Ω_p, Biot's (1941) consolidation equations in the frequency-space domain respond to

$$-\nabla \cdot \mathbf{T} = 0, \tag{1}$$

$$\nabla \cdot \mathbf{T}_f = j\omega \frac{\eta}{\kappa} \mathbf{w}, \tag{2}$$

where we use the sign convention for which the time derivative operator is equal to the factor "$+j\omega$" in the frequency domain, with j denoting the imaginary unit, $\omega = 2\pi f$ the angular frequency, and f the frequency; η is the dynamic viscosity of the pore fluid, κ the permeability, and $\mathbf{w}$ the displacement vector of the pore fluid relative to the solid skeleton. For small deformations of the porous medium in response to passing seismic waves, we can use the linear approximation $\mathbf{w} = \phi(\mathbf{U} - \mathbf{u})$ (Biot, 1962), where ϕ denotes the porosity, and $\mathbf{U}$ and $\mathbf{u}$ are the absolute displacement vectors of the particles of the pore fluid and the solid matrix, respectively. The total stress tensor $\mathbf{T}$ and the pore fluid stress $\mathbf{T}_f$ in the porous medium can be expressed as (Biot, 1941)

$$\mathbf{T} = \left[\left(K_b - \frac{2}{3}\mu_b + \alpha^2 M\right)\nabla \cdot \mathbf{u} - \alpha M \zeta\right]\mathbf{I} + 2\mu_b \mathbf{E}, \tag{3}$$

$$\mathbf{T}_f = M(\alpha \nabla \cdot \mathbf{u} - \zeta)\mathbf{I}, \tag{4}$$

where $\mathbf{I}$ is the identity tensor, $\mathbf{E} = \frac{1}{2}[\nabla \mathbf{u} + (\nabla \mathbf{u})^{\mathrm{T}}]$ the second-order elastic strain tensor, $\zeta = -\nabla \cdot \mathbf{w}$ a measure of the local change in the fluid content, μ_b the shear modulus of the poroelastic medium, and K_b the bulk modulus of the dry porous matrix. Recall that $\mathbf{T}_f = -P_f \mathbf{I}$, with P_f denoting the pressure of the pore fluid. The Biot-Willis constant α and the fluid storage coefficient M are defined as

$$\alpha = 1 - \frac{K_b}{K_s}, \tag{5}$$

$$\frac{1}{M} = \frac{\alpha - \phi}{K_s} + \frac{\phi}{K_f}, \tag{6}$$

where K_s and K_f are the bulk moduli of the solid grains and the pore fluid, respectively.

In the fluid domain Ω_f, we assume that the frequencies of seismically induced fluid displacements are sufficiently low so that we can ignore acceleration terms as well as the bulk viscosity of the fluid. Thus, we consider the linearized quasi-static NS equations (Landau & Lifshitz, 1959; Quintal et al., 2016)

$$\nabla \cdot \boldsymbol{\sigma}^f = 0\,, \tag{7}$$

where $\boldsymbol{\sigma}^f$ is the stress tensor of the fluid in Ω_f. The constitutive relation of the fluid, accounting for the viscosity and compressibility, responds to (Landau & Lifshitz, 1959; Quintal et al., 2016)

$$\boldsymbol{\sigma}^f = -p\mathbf{I} - \frac{2}{3}j\omega\eta(\nabla \cdot \mathbf{u}^f)\mathbf{I} + 2j\omega\eta\mathbf{E}^f, \tag{8}$$

where the vector $\mathbf{u}^f$ denotes the displacement of the fluid, $\mathbf{E}^f = \frac{1}{2}(\boldsymbol{\nabla}\mathbf{u}^f + (\boldsymbol{\nabla}\mathbf{u}^f)^{\mathrm{T}})$ is the strain tensor, p is the in-situ pressure of the fluid, which can be explicitly expressed in terms of the fluid displacement vector as

$$p = -K_f \nabla \cdot \mathbf{u}^f. \tag{9}$$

Equations (7) to (9) can be used to describe the laminar flow behavior of a Newtonian fluid. By substituting equations (8) and (9) into equation (7), one can obtain a more compact form of NS equations expressed in terms of fluid displacement variables only. This displacement form of NS equations will be used for the numerical implementation because of its inherent computational efficiency.

Considering the interaction between the fluid inclusions and the embedding porous background, coupling between the fluid domain Ω_f and the poroelastic domain Ω_p can be achieved by imposing the following interface conditions along Γ_{pf}:

1) Requiring mass conservation implies (Ager et al., 2019a, 2019b)

$$\mathbf{u}^f \cdot \mathbf{n}_f = (\mathbf{u} + \mathbf{w}) \cdot \mathbf{n}_f, \tag{10}$$

where $\mathbf{n}_f$ is an outward-directed unit vector normal to the fluid boundary.

2) Assuming that there is no-slip between the porous background and the fluid inclusions, this can be expressed as (Ager et al., 2019a, 2019b)

$$[\mathbf{u}^f - (\mathbf{u} + \mathbf{w})] \cdot \mathbf{t}_f = 0, \tag{11}$$

where $\mathbf{t_f}$ is the tangential unit vector on the fluid boundary. Please notice that other conditions are conceivable to allow for more detailed descriptions of relative motion between fluid inclusions and a poroelastic background. For example, Beavers & Joseph (1967) pointed out that a fluid in contact with a porous medium tends to flow faster at the interface than in the porous medium. This particular behavior is related with the fact that the interface separating the two media is difficult to define, and the porous system is a mixture of fluid and solid grains (Badia et al., 2009). The impact of these additional complexities will be explored in future works.

3) Requiring that the stress of the porous medium is balanced by the stress of the fluid (Ager et al., 2019a, 2019b)

$$\boldsymbol{\sigma}^f \cdot \mathbf{n}_f = -\mathbf{T} \cdot \mathbf{n}_p, \tag{12}$$

where $\mathbf{n}_p$ is an outward-directed unit vector normal to the poroelastic boundary. At the coupling interface Γ_{pf}, it is noted that $\mathbf{n}_f = -\mathbf{n}_p$.

4) Normal component of stress applied by the fluid being balanced by pressure of pore fluid implies (Ager et al., 2019a, 2019b)

$$\mathbf{n}_f \cdot (\boldsymbol{\sigma}^f \cdot \mathbf{n}_f) = -P_f \equiv \mathbf{n}_p \cdot (\mathbf{T}_f \cdot \mathbf{n}_p). \tag{13}$$

Equations (1) to (9), together with the coupling conditions (10) to (13), fully describe the physical behavior of the considered poroelastic samples containing mesoscopic-scale fluid inclusions.

Equations (10) to (13) describe the coupling between a fluid and a porous medium. As in our work the behavior of the latter is governed by Biot's theory, which cannot explicitly handle microscopic features, potential microscopic details of the interface should be neglected when using equations (10) to (13). This scale limitation of the interface conditions is similar to that mentioned by Gurevich & Schoenberg (1999) when deriving conditions for an interface separating two fluid-saturated porous media. In addition, the interface conditions describe an open-pore scenario, that

is, we assume that the inclusions and the porous background are hydraulically connected. In practice, scenarios involving partially connected or fully sealed interfaces are also conceivable, as, for example, clays or fines may clog the pores in the vicinity of the interfaces between the fluid inclusions and the poroelastic background (Gurevich & Schoenberg, 1999). In future works, we will consider the partially open and sealed interface cases and analyze the effects of interface hydraulic connectivity on the seismic signatures.

2.2 Oscillatory Relaxation Tests

Mesoscale fluid inclusions often exhibit complicated geometries, orientations, and distributions. As a result, seismic signatures, such as phase velocity and attenuation, usually show anisotropic characteristics. Following Rubino et al. (2016), we apply two compressive oscillatory relaxation tests and one shear relaxation test on a corresponding REV in order to calculate the effective anisotropic response of a 2D medium of interest. For each test, boundary conditions, similar to those provided by Rubino et al. (2016), are assigned at the outer edges of the REV (Figure 1c). While, due to the immense computational cost of 3D simulations, we limit the current study to 2D, it is important to note that the extension of the proposed methodology to 3D is conceptually straightforward. The governing equations (1) to (13) would remain the same and, for the upscaling procedure, one can follow the 3D generalization presented by Jian et al. (2021) for poroelastic media.

For mathematical simplicity, we define the corresponding outer boundaries of a rectangular REV as $\Gamma = \Gamma_T \cup \Gamma_B \cup \Gamma_L \cup \Gamma_R$, where Γ_T, Γ_B, Γ_L and Γ_R refer to the top, bottom, left, and right boundaries, respectively. The three tests and corresponding BCs used are summarized as follows.

- Compressive oscillatory relaxation test in vertical direction. This is achieved by imposing the following BCs:

$$\mathbf{u} \cdot \mathbf{n}_p = -\Delta \mathrm{u}, \qquad (x, y) \in \Gamma_T \cup \Gamma_B, \tag{14}$$

$$\mathbf{u} \cdot \mathbf{n}_p = 0, \qquad (x, y) \in \Gamma_L \cup \Gamma_R, \tag{15}$$

$$\left(\mathbf{T}\mathbf{n}_p\right) \cdot \mathbf{t}_p = 0, \qquad (x, y) \in \Gamma, \tag{16}$$

$$\mathbf{w} = 0, \qquad (x, y) \in \Gamma, \tag{17}$$

where $\mathbf{t}_p$ is the unit tangent on Γ.

- Compressive oscillatory relaxation test in horizontal direction. This is achieved by imposing the following BCs:

$$\mathbf{u} \cdot \mathbf{n}_p = -\Delta u, \qquad (x, y) \in \Gamma_L \cup \Gamma_R, \tag{18}$$

$$\mathbf{u} \cdot \mathbf{n}_p = 0, \qquad (x, y) \in \Gamma_T \cup \Gamma_B, \tag{19}$$

$$(\mathbf{T}\mathbf{n}_p) \cdot \mathbf{t}_p = 0, \qquad (x, y) \in \Gamma, \tag{20}$$

$$\mathbf{w} = 0, \qquad (x, y) \in \Gamma. \tag{21}$$

- Shear oscillatory relaxation test. This is achieved by imposing the following BCs:

$$\mathbf{u} \cdot \mathbf{t}_p = \Delta u, \qquad (x, y) \in \Gamma_T \cup \Gamma_B, \tag{22}$$

$$\mathbf{u} \cdot \mathbf{t}_p = 0, \qquad (x, y) \in \Gamma_L \cup \Gamma_R, \tag{23}$$

$$(\mathbf{T}\mathbf{n}_p) \cdot \mathbf{n}_p = 0, \qquad (x, y) \in \Gamma, \tag{24}$$

$$\mathbf{w} = 0, \qquad (x, y) \in \Gamma. \tag{25}$$

By solving the coupled system of equations under the above boundary conditions for each of the three oscillatory tests, we can compute the averaged stress and strain tensor components over the REV, which allows us to calculate its effective anisotropic viscoelastic stiffness matrix. For the considered 2D case under plain strain conditions, the generalized anisotropic stress-strain relationship can be expressed as (Rubino et al., 2016)

$$\begin{bmatrix} \langle \sigma_{11} \rangle \\ \langle \sigma_{22} \rangle \\ \langle \sigma_{12} \rangle \end{bmatrix} = \begin{bmatrix} C_{11} & C_{12} & C_{16} \\ C_{12} & C_{22} & C_{26} \\ C_{16} & C_{26} & C_{66} \end{bmatrix} \begin{bmatrix} \langle \varepsilon_{11} \rangle \\ \langle \varepsilon_{22} \rangle \\ \langle \varepsilon_{12} \rangle \end{bmatrix}, \tag{26}$$

where $\langle \sigma_{ij} \rangle$ and $\langle \varepsilon_{ij} \rangle$ denote the volume averages of the stress and strain components, and $\boldsymbol{C}$ is a complex-valued and frequency-dependent stiffness matrix. Unlike in Rubino et al. (2016), who employed a fully poroelastic framework, we are dealing with the coupled fluid-poroelastic problem and, thus, it is important to define the averaged stress and strain components that need to be used in equation (26). The averaged stress components can be expressed as

$$\langle \sigma_{ij} \rangle = \frac{1}{S} \left(\int_{\Omega_p} T_{ij} \, d\Omega + \int_{\Omega_f} \sigma_{ij}^f \, d\Omega \right), \tag{27}$$

where S is the area of the REV. With respect to the averaged strain over the sample, the context of this work highlights that the contribution of the poroelastic regions to this quantity is not obvious. In previous works performed in a fully poroelastic context, $\langle \varepsilon_{ij} \rangle$ was simply the spatial average of Biot's definition of solid strain component E_{ij} (e.g., Rubino et al., 2016). However, this strain tensor contains only information on the displacement of the solid phase. Recall that even though the behavior of the sample in response to a relaxation test is obtained in the context of poroelasticity, the interpretation of the results is made in a viscoelastic context and, then, there is no clear reason as to why the deformation should be quantified using Biot's definition of solid strain. Indeed, it seems to be more appropriate to use an average displacement field $\mathbf{u}_{pm}$ to approximate the deformation of the pore fluid-solid matrix system, that is,

$$\boldsymbol{\varepsilon}^{pm} = \frac{1}{2}\left[\left(\boldsymbol{\nabla}\mathbf{u}_{pm}\right) + \left(\boldsymbol{\nabla}\mathbf{u}_{pm}\right)^{\mathrm{T}}\right], \tag{28}$$

where $\mathbf{u}_{pm} = (1-\phi)\mathbf{u} + \phi\mathbf{U} = \mathbf{u} + \mathbf{w}$. Again, it is noted that the approximation is accurate as long as the deformation of the medium due to the passing of seismic waves is sufficiently small. Based on this approximation, the average strain of the sample can be expressed as

$$\langle \varepsilon_{ij} \rangle = \frac{1}{S}\left(\int_{\Omega_p} \varepsilon_{ij}^{pm}\, d\Omega + \int_{\Omega_f} E_{ij}^{f}\, d\Omega\right). \tag{29}$$

Note that this approximation of strain is only used to estimate the overall averaged strain in the sample. However, we remark the following important aspects for this approximation. First, this new approximation of averaged strain accounting for the contribution of both solid and fluid phases in the poroelastic domain is reconcilable with the definition of the averaged stress in equation (27), where the total stress, rather than the solid stress, components T_{ij} are used for the poroelastic domain. In addition, the approximation in equations (28) and (29) is compatible with the interface conditions (equations (10) and (11)) imposed on the displacement fields at the contact between the porous background and the fluid inclusions and, thus, the resulting average strain $\langle \varepsilon_{ij} \rangle$ equals the values computed using the displacements imposed at the outer boundaries of the sample, as expected and demonstrated in Appendix A. Moreover, this new approximation of strain is compatible with energetic considerations in the original heterogeneous, porous material. To support this, we introduce an independent energy-based approach (Solazzi et al., 2016) in section 2.3, which calculates seismic attenuation using the Biot's (1962) definitions of dissipation power

and strain energy, but not using the dynamic-equivalent viscoelastic medium assumption. Note that in Biot's (1962) definition of strain energy, the contribution of the pore-fluid pressure is also included. For the considered coupled NS-Biot problem, this new approximation of equivalent strain, as opposed to Biot's (1962) definition of solid strain, provides results that are consistent with those using the independent energy-based approach (Appendix B). Finally, it should be noted that, in a purely poroelastic context and due to the periodicity usually imposed on the fluid flow at opposite boundaries of the sample, Biot's (1962) definition of strain E_{ij} (equation (3)) and that proposed in this work (equation (28)) provide the same averaged strain and, thus, the same effective seismic characteristics (Appendix B).

The relationship established by equation (26) holds for the three oscillatory relaxation tests applied. This implies that we have nine equations and six unknowns (C_{ij}, with $i \leq j$). Following Rubino et al. (2016), we obtain the components of the effective stiffness matrix **C** through a least-squares procedure. Once these elements have been retrieved, it is possible to compute the effective complex-valued as well as frequency- and angle-dependent wavenumber k_{qP} and k_{qS} for quasi-*P*- (*qP*) and quasi-*S*-waves (*qS*) (Rubino et al., 2016). The corresponding phase velocity and inverse quality factor as functions of frequency and incidence angle θ can be calculated using

$$V_{qP,qS}(\omega,\theta) = \frac{\omega}{\mathcal{R}\left(k_{qP,qS}(\omega,\theta)\right)}, \tag{30}$$

$$\frac{1}{Q_{qP,qS}(\omega,\theta)} = -\frac{\mathcal{I}\left(k_{qP,qS}(\omega,\theta)^2\right)}{\mathcal{R}\left(k_{qP,qS}(\omega,\theta)^2\right)}, \tag{31}$$

where $\mathcal{R}$ and $\mathcal{I}$ refer to the real and imaginary parts, respectively.

2.3 Local Energy Dissipation

When studying seismic attenuation mechanisms, it is, in some cases, necessary to identify where, at a given frequency, the energy dissipation is taking place inside the probed sample. Following Solazzi et al. (2016), we therefore quantify the local contribution to the inverse quality factor, which is also referred to as the inverse quality factor density. For this, we first define several frequency-dependent functions. In the fluid domain Ω_f, the local dissipation power averaged over one wave cycle for a considered computational cell Δ_n of area δ_n^2 is given by (Lissa et al., 2020)

$$\langle \Delta \mathcal{P}^f(\omega)_n \rangle = 2\mu_f \omega^2 \mathcal{R}\left[\left(E_{11}^f E_{11}^{f*} + E_{22}^f E_{22}^{f*} + E_{12}^f E_{12}^{f*}\right) - \frac{1}{3}\left(E_{11}^f + E_{22}^f\right)\left(E_{11}^{f*} + E_{22}^{f*}\right)\right]_n \delta_n^2, \quad (32)$$

where the superscripts f and the asterisk (*) denote the fluid domain and the complex conjugate, respectively. In the poroelastic domain Ω_p, the local dissipation power in a cell Δ_m of the domain responds to (Rubino et al., 2016; Solazzi et al., 2016)

$$\langle \Delta \mathcal{P}^p(\omega)_m \rangle = \frac{\omega^2}{2}\left(\frac{\eta}{\kappa}\|\mathbf{w}(\mathrm{x},\mathrm{y})\|^2\right)_m \delta_m^2, \quad (33)$$

where the superscript p refers to the poroelastic domain Ω_p. In addition, the total strain energy function $\langle \mathcal{W}(\omega) \rangle$ of the REV is

$$\langle \mathcal{W}(\omega) \rangle = \sum_n \langle \mathcal{W}^f(\omega)_n \rangle + \sum_m \langle \mathcal{W}^p(\omega)_m \rangle, \quad (34)$$

where $\langle \mathcal{W}^f(\omega)_n \rangle$ and $\langle \mathcal{W}^p(\omega)_m \rangle$ are the strain energy functions for the fluid domain Ω_f and for the poroelastic domain Ω_p, respectively. They can be calculated using (Biot, 1962; Lissa et al., 2020; Rubino et al., 2016; Solazzi et al., 2016)

$$\langle \mathcal{W}^f(\omega)_n \rangle = \frac{1}{4}\mathcal{R}\left(\sigma_{11}^f E_{11}^{f*} + \sigma_{22}^f E_{22}^{f*} + 2\sigma_{12}^f E_{12}^{f*}\right)_n \delta_n^2, \quad (35)$$

$$\langle \mathcal{W}^p(\omega)_m \rangle = \frac{1}{4}\mathcal{R}\left[\left(T_{11}E_{11}^* + T_{22}E_{22}^* + 2T_{12}E_{12}^*\right) + P_f \zeta^*\right]_m \delta_m^2. \quad (36)$$

Note that, in equation (36), the contribution of the pore fluid pressure to the strain energy is considered. We can now define the inverse quality factor density in terms of average power dissipation density and strain energy functions as (Solazzi et al., 2016)

$$q^{-1}(\omega) = \frac{\langle \Delta \mathcal{P}(\omega) \rangle}{2\omega\delta^2 \langle \mathcal{W}(\omega) \rangle}, \quad (37)$$

which will be used to study the wave attenuation mechanism. The summation of inverse quality factor density in equation (37) over the entirety of the probed sample then results in the inverse quality factor at a given frequency

$$Q^{-1}(\omega) = \sum_{\Omega_p + \Omega_f} q^{-1}(\omega)\delta^2. \quad (38)$$

2.4 Numerical Implementation

In the preceding sections, we presented the set of equations that permit to describe a coupled fluid-poroelastic model as well as three associated oscillatory relaxation tests to obtain the upscaled

response of the medium. To solve this set of equations, we employ the "mathematical module" in the finite-element-based software COMSOL Multiphysics. We use unstructured triangular meshes, which allow for an efficient discretization of narrow features, such as fractures or fluid channels. For the fluid domains and in their vicinities, we employ sufficiently fine meshing to accurately capture the FPD effect in and near the fluid-poroelastic interface. Moreover, we use quadratic Lagrange shape functions for both solid and relative fluid displacement variables of Biot's equations in the poroelastic domain. For the NS equations, quadratic shape functions are used for fluid displacement variables. The discretized problem is solved using the direct parallel solver MUMPS in the frequency domain, which readily enables us to evaluate the velocity dispersion and attenuation spectra of seismic waves in the probed medium.

3 Results

In this section, we verify the effectiveness of the proposed approach using two numerical examples. First, we analyze two orthogonal fractures embedded in a poroelastic background. We assess the correctness of the proposed coupled fluid-poroelastic approach by comparing it with two widely used numerical upscaling schemes. One is the purely poroelastic approach (Rubino et al., 2016), in which both the background and fractures are characterized using the Biot's equations. The other is the coupled fluid-elastic approach (Quintal et al., 2019), where the fractures are similarly characterized by the NS equations, while the dynamic behavior of the background is characterized using the quasi-static elastic equations. Then, we compare the three approaches considering the influence of material properties as well as fracture apertures. In the second example, we investigate the seismic attenuation and velocity dispersion of a synthetic carbonate-type sample containing mesoscopic vugs embedded in a microscopic porous matrix.

3.1 Comparison with Previous Approaches

We consider a square REV with a side length of 0.2 m (Figure 2a) that contains two interconnected orthogonal fractures orientated along the vertical and horizontal axes. The poroelastic background medium is characterized by physical properties representative of a stiff quartz sandstone. We assume that both the background and the fractures are fully saturated with water. The corresponding physical rock and fluid properties are summarized in Table 1 (Bourbié et al., 1987; Rubino et al., 2016). A schematic view of the mesh employed in the finite element simulations is

provided in Figure 2b. The mesh is refined near the boundaries of the fractures to correctly represent FPD processes. Note that for the considered model, in both the purely poroelastic approach and the proposed coupled fluid-poroelastic approach, two attenuation peaks are expected, which correspond to fracture-to-background (FB) FPD and fracture-to-fracture (FF) FPD (Rubino et al., 2013). However, the coupled fluid-elastic approach can only predict one attenuation peak associated with FF-FPD effect. For the attenuation peak due to FB-FPD, the characteristic frequency of the associated maximum attenuation is directly proportional to the background permeability, while, for the attenuation peak due to FF-FPD, the characteristic frequency is directly proportional to the fracture permeability and inversely proportional to the length of the fractures (Rubino et al., 2017).

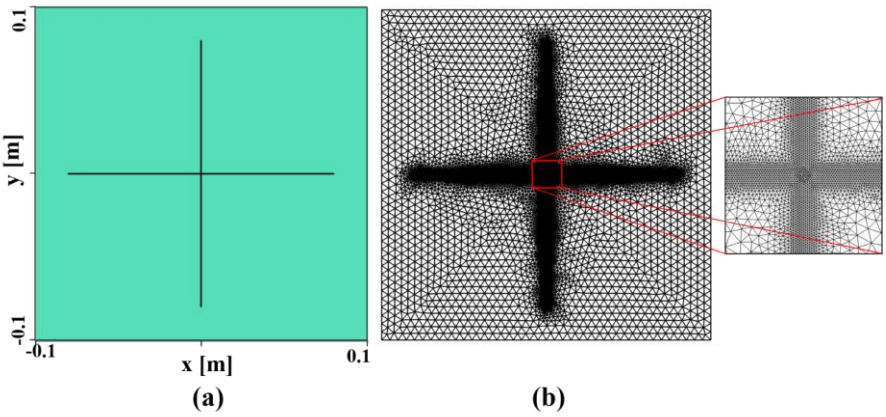

Figure 2. (a) Canonical fracture model and (b) its discretization.

Table 1. Physical properties of background rock and pore fluid.

Background rock	Value
Grain density ρ_s (kg/m^3)	2650
Grain bulk modulus K_s (GPa)	37
Porosity ϕ	0.04
Drained bulk modulus K_b (GPa)	26
Drained shear modulus μ_b (GPa)	31
Permeability κ(D)	0.01
Fluid phase	
Density ρ_f (kg/m^3)	1090

Bulk modulus K_f (GPa)	2.25
Viscosity η (Pa $\cdot$ s)	0.001

3.1.1 Seismic Attenuation and Phase Velocity Dispersion

To validate the newly proposed method for computing seismic attenuation and phase velocity dispersion of porous rocks containing fluid-filled voids in the mesoscopic scale range, we compare our results with those obtained using a purely poroelastic approach (Rubino et al., 2016) and also with those using a coupled fluid-elastic approach (Quintal et al., 2019). For the coupled fluid-elastic approach, the poroelastic background is approximated with an equivalent elastic solid, for which the effective bulk K_e and shear moduli μ_e are calculated using the Gassmann's (1951) equations: $K_e = K_b + \alpha^2 M$ and $\mu_e = \mu_b$. The effective density is obtained using $\rho_e = \rho_s(1 - \phi) + \rho_f \phi$. On the other hand, when using the purely poroelastic approach to represent fluid-filled voids, we need to determine the corresponding effective properties of the porous material representing them. For example, the permeability of the fracture has to be specified, whereas in the proposed approach, the permeability is controlled by the geometrical characteristics of the corresponding voids. Using the coupled fluid-elastic approach, Quintal et al. (2019) already showed that, if appropriate material properties are used for the fractures, the two solutions should be identical, at least with regard to FF-FPD effects. For the comparison, we assume that, at the grain level, the physical properties of the fractures in the fully poroelastic model are the same as those of the embedding background. With respect to the dry frame properties, as we intend to represent mesoscopic void inclusions in a poroelasticity framework, we use a porosity value $\phi = 0.999$, which in turn, implies very low values of bulk and shear moduli. To choose these values, we have checked that when K_b and μ_b are reduced to values that are much lower than the fluid bulk modulus, the results of the purely poroelastic approach converge to those provided by the proposed coupled approach. However, we cannot further reduce these moduli, otherwise, numerical instabilities can occur. Therefore, in our work, we use $K_b = \mu_b = 3 \times 10^5$ Pa. Given that each fracture has a rectangular geometry, with a constant aperture of $h = 3 \times 10^{-4}$ m and a length of 0.16 m, we estimate the permeability of the porous material representing the fractures using the so-called cubic law $\kappa = h^2 \, / \, 12$ (e.g., Jaeger et al., 2007). In this context, it is important to notice that for the model considered, the two attenuation peaks are clearly separated in the

frequency domain. This implies that near the characteristic frequency of the attenuation peak due to the fracture-to-fracture FPD, the induced fluid flow is restricted within the fractures and fluid flow between fractures and porous background is negligible. Therefore, the cubic law provides accurate estimation of fracture permeability. Using these material properties, the velocity dispersion and attenuation characteristics of both *qP*- and *qS*-waves are calculated using the three approaches. In doing so, we consider propagation angles θ with respect to the vertical of 0° and 45°. The corresponding results are shown in Figure 3 for frequencies ranging from 1 to 10^7 Hz.

We first compare the proposed coupled fluid-poroelastic approach and the purely poroelastic approach. For $\theta = 0°$, the *qP*-wave exhibits significant phase velocity dispersion (Figure 3a) presenting two inflections associated with FB-FPD and FF-FPD. Correspondingly, the Q^{-1}-spectra show two attenuation peaks (Figure 3b). For $\theta = 45°$, we observe only one attenuation peak of the *qP*-wave in the low-frequency range due to FB-FPD (Figure 3b). The attenuation peak due to the FF-FPD is not present due to the symmetry of the fracture network since, in this case, both horizontal and vertical fractures are compressed equally by the passing *qP*-wave and experience a similar fluid pressure increase. For both propagation angles, the two approaches provide quite consistent results, with the maximum relative differences of phase velocity for the two methods being less than 0.2%. Figures 3c and 3d illustrate the corresponding behavior of the *qS*-wave. This wave mode exhibits very little dispersion and attenuation for $\theta = 0°$ due to the intrinsic geometry of the system. However, for $\theta = 45°$, the attenuation related to FB-FPD is insignificant, while we observe rather pronounced attenuation due to FF-FPD. For the latter, the fluid pressures in the two fractures have opposite signs because the deformation induced by the *qS*-wave extensional in one of the fractures and compressional in the other. Therefore, the corresponding pressure gradient becomes very large between the two fractures (Rubino et al., 2017). Again, the results are in quite good agreement for the two approaches, and the maximum relative difference of *qS*-wave velocity for the two approaches is less than 0.7%.

When the coupled fluid-elastic approach is used, we observe consistent results only in the high-frequency range where FF-FPD controls the seismic attenuation and velocity dispersion. This further supports the effectiveness of the proposed coupled fluid-poroelastic approach. However,

as expected, no attenuation and velocity dispersion are observed in the low-frequency range, which is one of the intrinsic limitations of the coupled fluid-elastic approach.

In summary, the results obtained using the newly proposed coupled fluid-poroelastic approach to model seismic signatures of porous rocks containing mesoscopic fluid-saturated fractures shows good agreement with a fully poroelastic representation of the medium, provided that suitable poroelastic fracture properties are considered. This demonstrates the correctness of the proposed upscaling scheme for representing FPD between mesoscopic fluid-filled inclusions and the porous background as well as between the mesoscopic inclusions themselves. The comparison with the coupled fluid-elastic approach further supports the effectiveness of the proposed approach and highlights the contribution of this work.

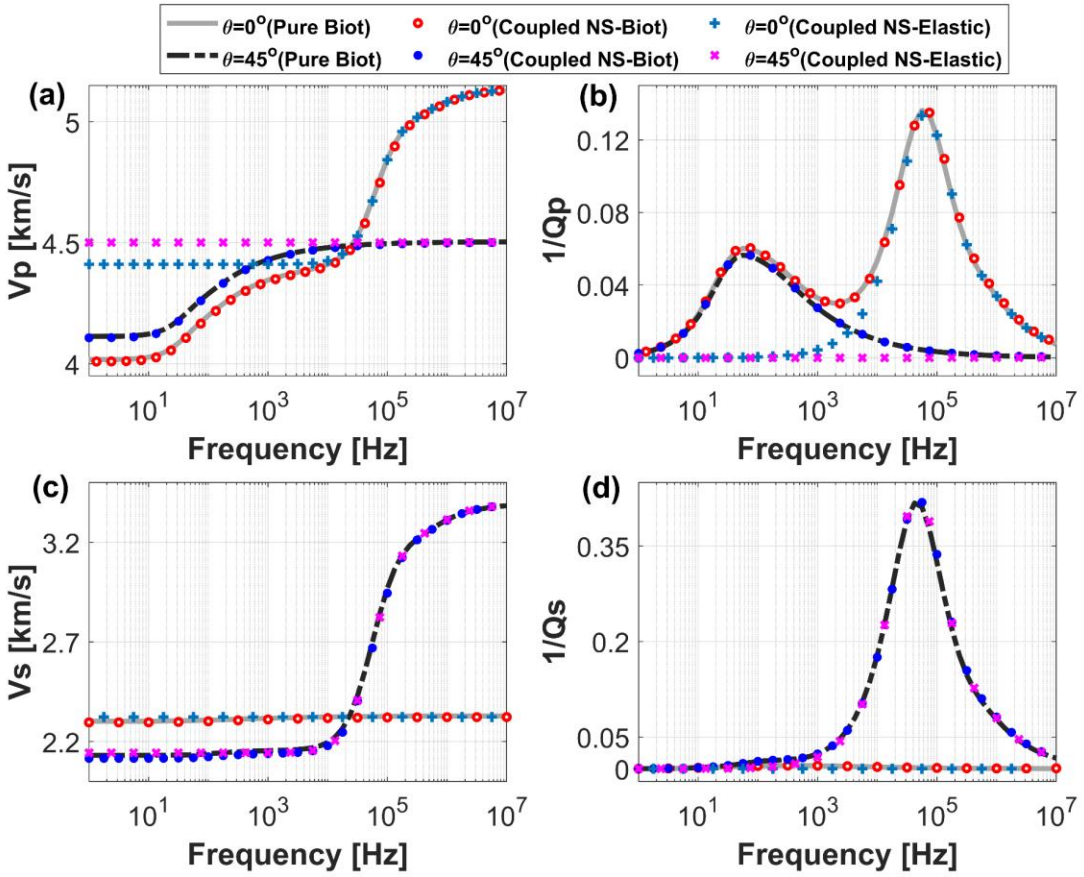

Figure 3. Comparison of *qP*-wave (a) phase velocity and (b) inverse quality factor and *qS*-wave (c) phase velocity and (d) inverse quality factor as functions of frequency for propagation angle θ of 0° and 45° with respect to the vertical. The results correspond to the fracture model shown in Figure 2. The "coupled NS-Biot" results are obtained using the proposed coupled fluid-poroelastic

approach; the "Pure Biot" results are obtained using the purely poroelastic approach (Rubino et al., 2016), where both the background and the fractures are characterized by the Biot's poroelastic equations (Biot, 1941); the "coupled NS-Elastic" results are obtained using the coupled fluid-elastic approach (Quintal et al., 2019), where the fractures are characterized using the NS equations, while the background is fully elastic with effective material parameters obtained using the Gassmann's (1951) equation.

3.1.2 Influence of Fracture Compliance in Purely Poroelastic Approach

As shown above, the proposed fluid-poroelastic approach to compute the seismic signatures of porous media containing mesoscopic fluid inclusions provides results that, in some cases, can also be obtained following a purely poroelastic approach by optimizing the material properties inside the fluid inclusions. As previously mentioned, this is due to the fact that Biot's (1941) equations involve more parameters when representing fluid inclusions, which may lead to ambiguity in their identification from seismic data. In the following, we investigate the influence of the drained bulk and shear moduli which are needed in the purely poroelastic approach to model the mesoscopic fluid-filled fractures. To this end, we analyze the response obtained using the purely poroelastic approach by varying the drained bulk modulus K_b for the fractures, which is a parameter that is not present in the proposed coupled fluid-poroelastic approach. In the simulations, the drained shear modulus μ_b is assumed to be equal to the drained bulk modulus K_b to facilitate the analysis. The remaining physical properties and geometrical parameters are identical to those employed in Section 3.1.1.

Figure 4 illustrates the spectra of phase velocity and inverse quality factor of the *qP*-wave for $\theta = 0°$ and of the *qS*-wave for $\theta = 45°$. We notice that the choice of the drained bulk and shear moduli has indeed a significant impact on the results, which, in relative terms, is more pronounced for the *qS*-wave (Figure 4d). For relatively small values of these moduli, the phase velocity curves converge to the same results as those obtained using the proposed coupled fluid-poroelastic approach (Figures 4a to 4d). However, when larger values of the drained bulk modulus are used, significant changes are observed in the low-frequency range. The optimal value for emulating the NS representation of the fractures is $K_b = \mu_b = 3 \times 10^5$ Pa. It should be noted that this optimized

value cannot be generalized for other scenarios, as it varies with the model geometry. Another observation regarding the attenuation spectra is that the peaks are shifted towards higher frequencies and their amplitude decreases when increasing the fracture drained bulk and shear moduli.

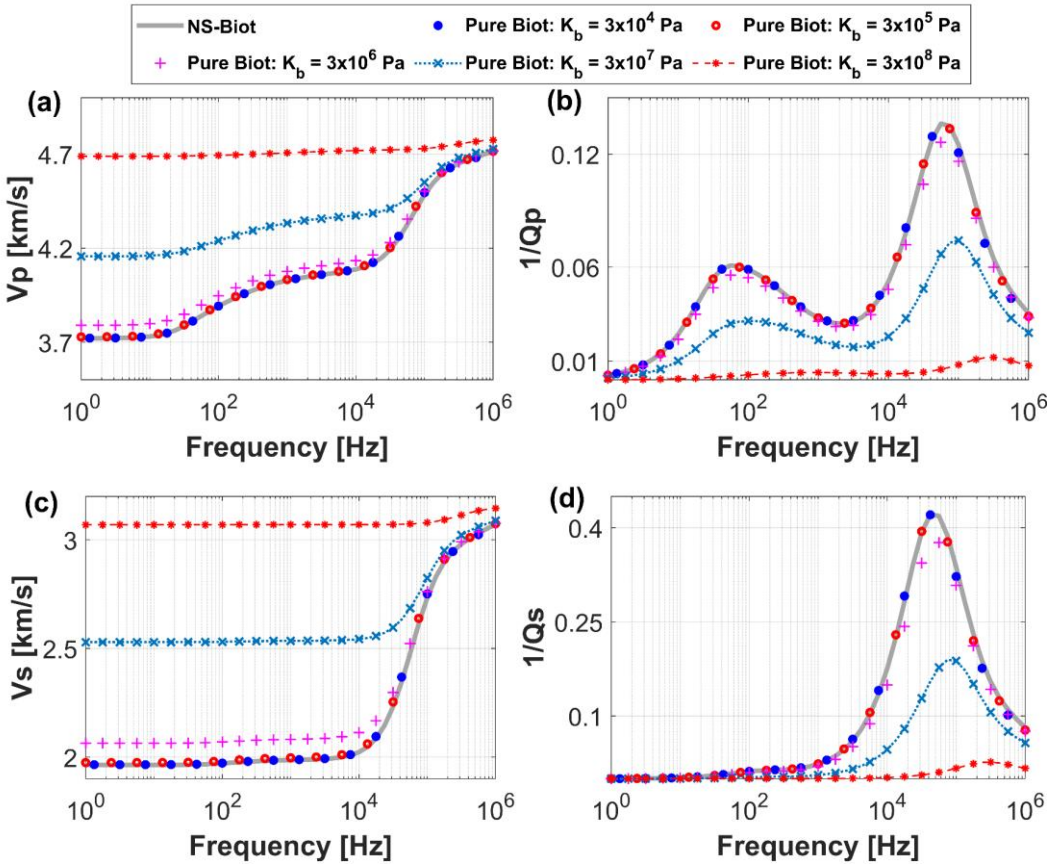

Figure 4. Influence of drained bulk and shear moduli of the fractures in the purely poroelastic approach on the *qP*-wave (a) phase velocity and (b) inverse quality factor as functions of frequency for propagation angle $\theta = 0°$. (c) Phase velocity and (d) inverse quality factor of the *qS*-wave for $\theta = 45°$. For all the simulations, the model is the same as that in Figure 2 and we set $\mu_b = K_b$ for simplicity. In the purely poroelastic approach, the permeability in the fracture is calculated using the cubic law.

For this comparison, we assume that the mesoscopic fractures are fully fluid-saturated. However, we note that, for heterogeneities of this kind containing porous infills, such as unconsolidated grains, the purely poroelastic approach remains a suitable option, because both the geometry of inclusions and the infill determine the hydromechanical properties of heterogeneous porous rocks.

3.1.3 Fracture Asperities

Natural fractures tend to exhibit complicated roughness along their walls, also known as asperities, which affect the FPD process and, thus, the hydraulic and mechanical properties of the fractured rock mass. For generic asperities, there is no analytical expression that can relate explicitly the permeability and the fracture aperture. Quintal et al. (2019) studied squirt flow effects in interconnected fractures with asperities and compared the coupled fluid-elastic approach with a purely poroelastic solution. However, they ignored the low-frequency peak associated with FB-FPD predicted by the Biot's (1941) poroelastic equations because the coupled fluid-elastic approach assumes no fluid exchange between the elastic background and the fracture fluid. Recently, Lissa et al. (2020) investigated squirt flow in more complicated fractures and arrived to the conclusion that seismic signatures are significantly influenced by the roughness of the crack walls. In this section, we revisit this problem and compare the three approaches for the full frequency range to analyze both FB- and FF-FPD effects.

To emulate asperities, we consider a fracture wall with a symmetrically constricted geometry. Apart from the asperities, the considered model is the same as that employed previously (Figure 2, Table 1). The local variation of the aperture is governed by a sinusoidal function except for the intersection between the two fractures. A unit cell of the considered fracture wall is illustrated in Figure 5, with δ and λ denoting the amplitude and wavelength, respectively, of the sinusoidal function, and d the mean aperture. For all simulations, we use $d = 0.3$ mm, $\delta = 0.2$ mm and $\lambda = 0.8$ mm, which results in a minimum and maximum aperture of $h_{min} = 0.1$ mm and $h_{max} = 0.5$ mm, respectively.

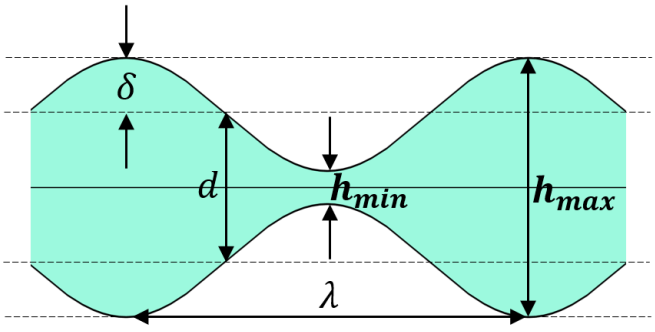

Figure 5. Schematic illustration of a unit cell of the considered fracture wall characterized by harmonic asperities.

We consider *qP*- and *qS*-waves with propagation angles θ of 0° and 45°, respectively. Figure 6 shows the phase velocity and the inverse quality factor as functions of frequency for the three approaches. Note that during the simulations, we keep the roughness of the fracture wall the same (Figure 5), but for the purely poroelastic approach, we use two different effective apertures (h_{min} and h_{max}) to estimate the fracture permeability using the cubic law. We can still observe two distinct attenuation peaks in the attenuation spectrum of the *qP*-wave when using the coupled fluid-poroelastic approach and purely poroelastic approach. Compared to the model with rectangular fractures (Figure 2), the attenuation peaks are shifted to lower frequencies, this effect being more pronounced for the high-frequency peak. For the first attenuation peak, the results of the proposed coupled fluid-poroelastic approach and the purely poroelastic approach considering the fracture asperities are almost identical (Figure 6). The characteristic frequency associated with the first peak is mainly controlled by the background permeability. In this sense, this attenuation peak related to FB-FPD is insensitive to the fracture permeability. Both the proposed coupled fluid-poroelastic approach and the purely poroelastic approach therefore predict similar values of seismic attenuation and velocity dispersion at the frequencies where the energy dissipation is controlled by the FB-FPD mechanism. Again, this attenuation is not predicted by the coupled fluid-elastic approach (Figure 6b). For the second attenuation peak, we see that the results of the proposed coupled fluid-poroelastic approach and the coupled fluid-elastic approach predict identical values for both *qP*- and *qS*-waves (Figures 6b and 6d). However, we observe some obvious differences in the characteristic frequency for the coupled fluid-poroelastic approach and the purely poroelastic approach, even though they provide similar magnitude of attenuation. The characteristic frequency predicted by the proposed coupled fluid-poroelastic approach and coupled fluid-elastic approach is 2×10^4 Hz, while for the purely poroelastic approach we get 4×10^3 Hz and ~10^5 Hz when the minimum and maximum apertures, respectively, are used to evaluate the effective permeability. As this second attenuation peak is an effect of FF-FPD, its characteristic frequency is influenced by the fracture permeability. Even for this simple scenario, the peak frequency of the purely poroelastic model can vary by more than one order-of-magnitude because of the uncertainty of equivalent aperture selection to determine the effective permeability. In practice, fracture networks tend to exhibit much more complicated aperture variations and

orientations. This renders the determination of an effective permeability for each fracture largely impossible, which, in turn, makes the use of the purely poroelastic approach impractical.

It is important to remark here that a similar model that considers the dynamic interaction between a fluid medium and a porous background has been previously proposed by Vinci et al. (2014a). The authors use a 1D solution of the NS equations for laminar flow to characterize the dynamic aspect within a fracture. Their approach is, however, incapable of dealing with fracture surfaces exhibiting asperities or multiple intersecting fractures due to the inherent assumptions of axial symmetry and the validity of the cubic law. These limitations were alleviated in our work by solving the quasi-static linearized NS equations (Landau & Lifshitz, 1959; Quintal et al., 2016). As shown in Figure 6, the employment of cubic law to estimate fracture permeability results in uncertainties and errors, while the proposed coupled fluid-poroelastic approach naturally accounts for the fracture permeability and provides reliable results. In Figures 3 and 6, we demonstrated the correctness of the proposed approach using a model with two interconnected and orthogonal fractures orientated in the vertical and horizontal directions. It is important to note that the proposed approach can be readily applied to multiple intersecting fractures with arbitrary inclination angles since the proposed scheme permits to calculate anisotropic characteristics of both *qP*- and *qS*-waves.

We analyzed above the influence of fracture asperities on the fracture permeability based on the fracture model given in Figure 5. However, it is important to mention that asperities could also have a strong impact on fracture compliance. Indeed, the fracture contact area density and distribution play a very important role in the stiffness of fractured rocks (Rubino et al., 2015; Lissa et al., 2020). In this context, it is important to notice that changes in effective fluid pressure of fractures may induce variation in contact density and distribution of asperities. When the pressure inside the fracture is increased, for example, due to fluid injection, the fracture aperture will increase and fractures will have only isolated regions of contact. Conversely, when the fluid pressure inside the fracture is decreased, for example due to production, the fracture aperture will decrease, and the contact area increases (Rubino et al., 2015). The change of contact areas has a significant impact on fracture permeability and compliance, which will result in variations of seismic attenuation as well as other seismic attributes. In the future, we intend to perform a

comprehensive analysis of fracture contact area effects on permeability and compliance and on the corresponding impact on WIFF in 3D configurations.

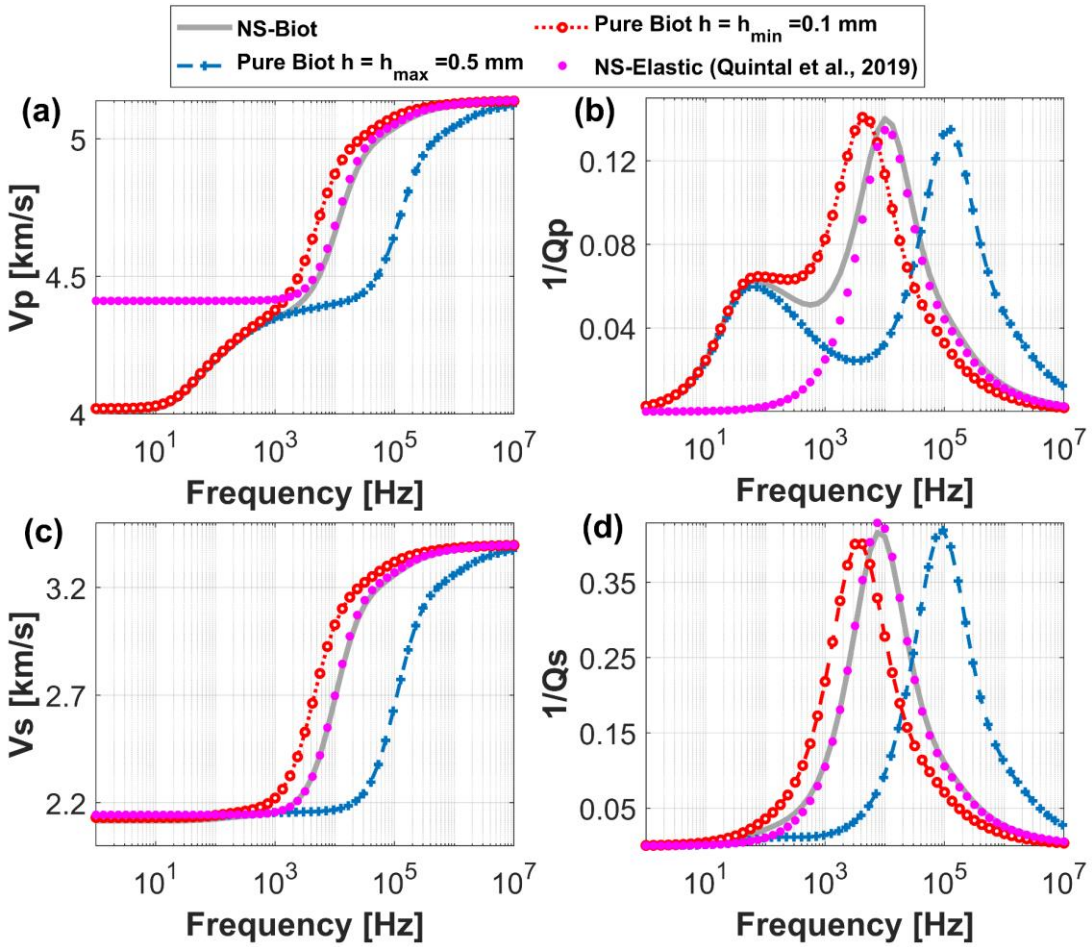

Figure 6. Comparison of *qP*-wave (a) phase velocity and (b) inverse quality factor as functions of frequency for $\theta = 0°$, and *qS*-wave (c) phase velocity and (d) inverse quality factor for $\theta = 45°$ obtained using three different approaches for a model of intersecting perpendicular fractures (Figure 2) with symmetric harmonically constricted walls (Figure 5). The "NS-Biot" results correspond to the proposed coupled fluid-poroelastic approach, "pure Biot" results to the purely poroelastic model (Rubino et al., 2016), and "NS-Elastic" to the coupled fluid-elastic approach (Quintal et al., 2019).

To corroborate the above analyses and to investigate the seismic attenuation mechanism, we calculate the inverse quality factor density corresponding to the frequency of the first and the second attenuation peaks in Figure 6b using the coupled fluid-poroelastic approach and the purely

poroelastic approach, respectively. Results for the first attenuation peak are illustrated in Figures 7a and 7b using a logarithmic scale. The two approaches provide very similar energy dissipation distributions with strong energy dissipation occurring mainly in the poroelastic background, being more pronounced near the fracture walls and particularly in the vicinity of the fracture tips. The results in Figures 7c and 7d correspond to the characteristic frequency of the second peak. We depict the inverse quality factor density near the intersection area where the energy dissipation is most representative and pronounced. We see that, for both approaches, energy dissipation mainly takes place at the narrowest regions of the fractures, where fluid flow is enhanced due to fluid mass conservation and a change in fracture cross section, while it is almost negligible in the poroelastic background. For the coupled approach, we observe minimal energy dissipation at the center of the fracture, and the maximum values at the fracture walls, where fluid velocity reaches its lowest values due to viscous friction (Figure 7c). For the purely poroelastic approach, the energy dissipation is more uniform in the narrowest regions (Figure 7d). Analyses of this kind are of relevance for applications, in which the location of maximal fluid shearing is relevant, such as, for example, studies regarding the mobilization of colloids and particles in response to FPD (e.g., Barbosa et al., 2019).

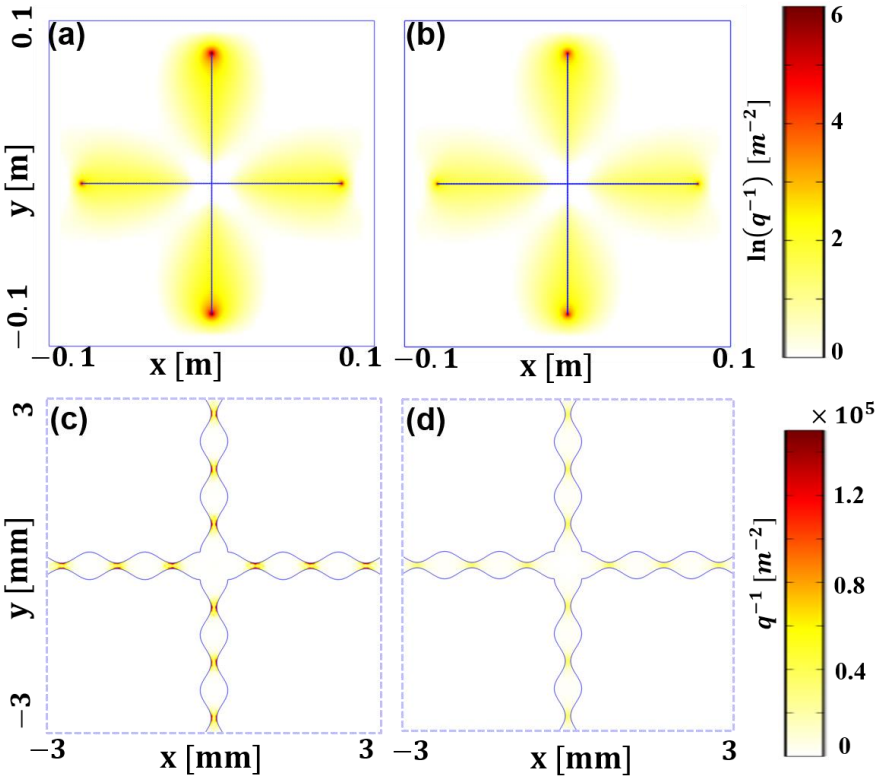

Figure 7. Distribution of inverse quality factor density for intersecting fractures with symmetric harmonically constricted walls. (a) and (b) correspond to the frequency of the first attenuation peak related to FB-FPD and (c) and (d) to that of the second attenuation peak related to FF-FPD shown in Figure 6b. (a) and (c) are based on the proposed coupled fluid-poroelastic approach, while (b) and (d) are based on the purely poroelastic approach. Note that the top panel is displayed in a logarithmic colorscale.

3.2 Application in a Vuggy Carbonate-type Sample

Porous and/or karstic carbonates play an important role in the oil and gas industry, accounting for ~60% of the global reserves (e.g., Burchette, 2012, Agada et al., 2016). Furthermore, carbonate aquifers provide drinking water to ~10% of the world's population (e.g., Goldscheider et al., 2020). One of the major challenges when studying carbonates is the correct characterization of their hydro-mechanical characteristics. In this sense, permeabilities of carbonates can vary several orders-of-magnitude for the same porosity and the pore sizes tend to exhibit an extreme variability ranging from the micro- all the way to the macroscale (e.g., Burchette, 2012). These distinctive properties of carbonates were analyzed by Anselmetti et al. (1998), who explored the relations between the local permeability and the associated size distributions of the pores, which were constituted of both micro- and mesopores in the micro- and millimeter scale ranges, respectively. Agersborg et al. (2009) showed that significant variations of the acoustic properties in carbonates can be explained by the effects of dual porosity and pore pressure communication. In a more recent work, Bailly et al. (2019) studied the elastic properties of carbonates based on a multiscale geophysical dataset obtained through seismic refraction surveying as well as sonic and ultrasonic measurements on outcrop samples. Their results indicate that mesoscale fluid inclusions have a considerable impact on *P*-wave velocities. However, as far as we know, there are, as of yet, no works assessing the effective seismic characteristics of carbonates accounting for complex fluid-filled mesopores in combination with a poroelastic background. In the following, we seek to overcome this limitation by applying the proposed coupled fluid-poroelastic upscaling scheme to a pertinent synthetic sample.

Inspired by the optical thin-section images of Anselmetti et al. (1998), we emulate the mesoscale voids of a synthetic carbonate-type sample using a binarized stochastic model based on a Gaussian

spectral density function. The considered REV is illustrated in Figure 8. The side length of the sample is 0.18 m. The model contains a number of mesoscale voids (green regions) embedded in a porous background (white region). The latter is constituted of a calcite matrix containing micropores and, as such, is represented by the Biot's (1941) equations. The characteristic size of the mesopores varies from hundreds of micrometers to several centimeters and they present a horizontal-to-vertical aspect ratio of 4. Within these mesopores, the NS equations are used to describe the motion of the saturating fluid.

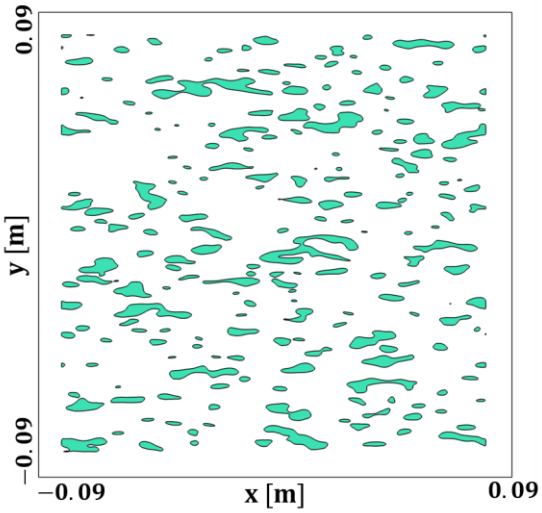

Figure 8. Synthetic carbonate-type sample containing mesoscale fluid-saturated voids (green) embedded in a poroelastic background (white).

For computing the effective seismic characteristics of this medium, we consider for the porous background that, at the grain scale, the elastic properties are those of pure calcite: $K_s = K_{calcite} = 71$ GPa, $\mu_s = \mu_{calcite} = 30$ GPa, and $\rho_s = \rho_{calcite} = 2710$ kg/m^3 (Mavko et al., 2009). For the porous matrix, we use typical values of microporosities and micropermeabilities of carbonate samples measured by Anselmetti et al. (1998): $\phi = 0.12$ and $\kappa = 0.1$ mD. The drained bulk and shear moduli are calculated employing the asymptotic expressions proposed by David and Zimmerman (2011), where the medium is assumed to contain dry circular pores. Using the values of grain moduli and the porosity, we get $K_b = 50.41$ GPa and $\mu_b = 23.54$ GPa. We assume that both the micropores and mesopores are fully saturated with water, the physical properties of which are summarized in Table 1. The model is discretized using unstructured triangular meshes, which are locally refined in the vicinity of the boundary of the fluid-filled voids.

The seismic velocity dispersion and attenuation spectra of the *qP*- and *qS*-waves are shown in Figure 9 for a range of incidence angles θ. For the *qP*-wave, we observe that, both the phase velocity and the inverse quality factor are dependent on the frequency and on the propagation angle (Figures 9a and 9b). In particular, the *qP*-wave shows very significant dispersion for vertical propagation. At the peak frequency $f = 7.5$ Hz, the Q_p -values are ~40. With increasing propagation angle, dispersion and attenuation decrease very rapidly and, for the horizontal propagation, become almost insignificant. Another observation is the high degree of *qP*-wave velocity anisotropy, which is more pronounced at low frequencies. The results of the *qS*-wave are depicted in Figures 9c and 9d. Again, we observe a distinct attenuation peak, for which the peak frequency is the same as that for the *qP*-wave. However, the dispersion of the *qS*-wave is weaker. In the case of horizontal and vertical propagation, the dispersion and attenuation of the *qS*-wave are largely insignificant. The most pronounced velocity dispersion and attenuation occur for a propagation angle of $\theta = 45^{\circ}$. The anisotropy associated with the propagation of the *qS*-wave is very small compared to that of the *qP*-wave.

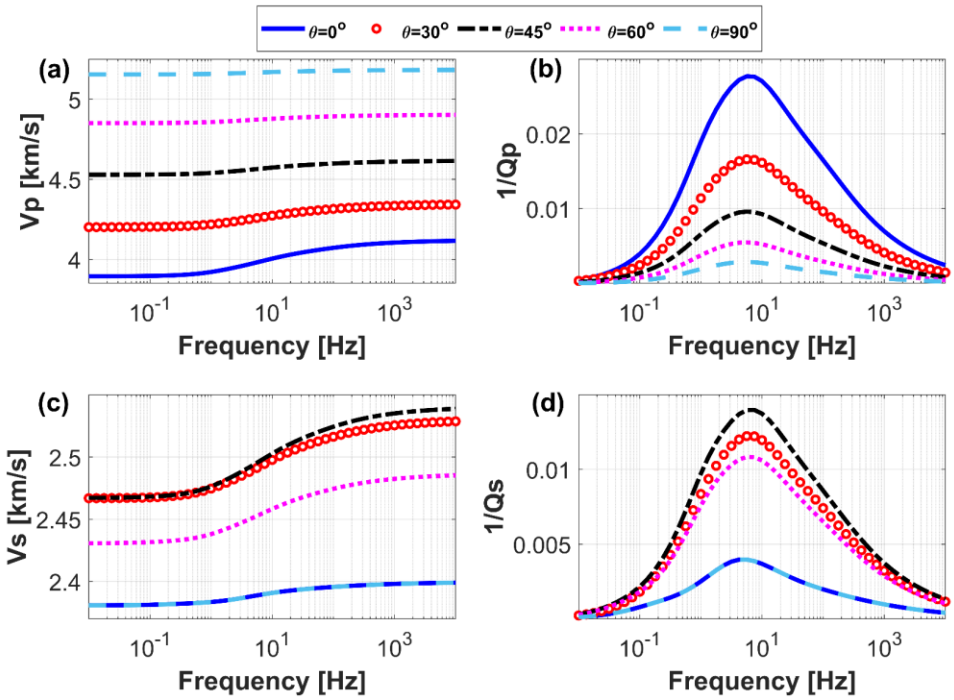

Figure 9. *qP*-wave (a) phase velocity and (b) inverse quality factor and *qS*-wave (c) phase velocity and (d) inverse quality factor as functions of frequency and propagation angle θ.

To understand the underlying mechanism of the observed seismic attenuation and velocity dispersion, we study the inverse quality factor density and the fluid pressure distributions in response to the oscillatory relaxation tests. For the considered carbonate sample, the coefficients C_{16} and C_{26} are much smaller than other components in the stiffness matrix (not shown here), which implies that it can be considered as a transversely isotropic medium. In this case, the vertical and horizontal compressibility tests can be associated with the *qP*-wave propagating with an angle θ of 0° and 90°, and the shear test corresponds to the *qS*-wave propagation in the vertical direction. Figure 10 illustrates the inverse quality factor density of both *qP*- and *qS*-waves at the frequency of the attenuation peak. In each case, we observe that the dissipation occurs mainly in the poroelastic background. For *qP*-wave propagation with $\theta = 90^{\circ}$ (Figure 10b), the spatial attenuation pattern is similar to that of $\theta = 0^{\circ}$ (Figure 10a), but the regions with significant energy dissipation are much smaller and are associated with lower values. This explains the reduction of attenuation observed in Figure 9 for $\theta = 90^{\circ}$. As expected, small values of quality factor density are also observed when the *qS*-wave propagates vertically (Figure 10c). For all these results, the attenuation is dominated by FPD between the larger mesopores and the embedding microporous background, while the contribution of the smaller voids is of subordinate importance. This is due to the fact that the compliance of larger voids is significantly higher than that of smaller ones.

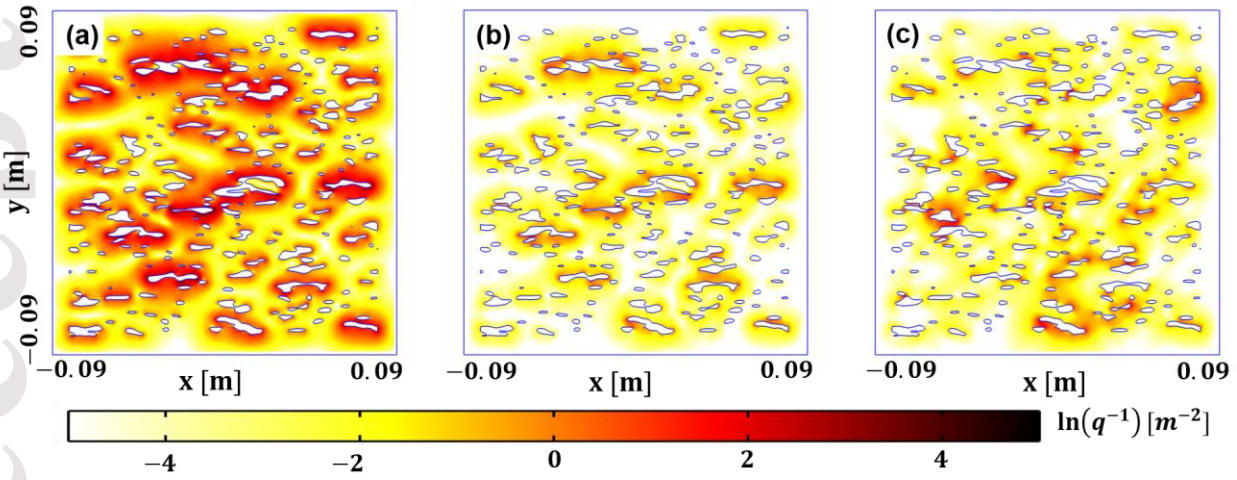

Figure 10. Distribution of the inverse quality factor density for the synthetic carbonate-type rock shown in Figure 8 at the frequency of the attenuation peak (Figures 9b and 9d). Results of the *qP*-wave propagation in (a) vertical direction, (b) horizontal direction; and (c) result of the *qS*-wave propagation in vertical direction.

To further explore the role played by the different pore sizes on the seismic response, we illustrate in Figure 11 the corresponding fluid pressure distributions. It is observed that, where energy dissipation is strong (Figure 10), there are relatively obvious pressure surges inside the corresponding fluid inclusions. Recall that the fluid inclusions and the poroelastic background are hydraulically connected. The seismic wave motion causes some of the mesoscopic voids to be strongly deformed due to their large compliances, which, in turn, increases the fluid pressure in the corresponding voids. Due to the thus arising pressure disequilibrium, fluid pressure communication takes place locally between the mesoscopic voids and the embedding microporous background. The diffusion of the fluid pressure in the poroelastic background leads to the observed local energy dissipation and resulting seismic attenuation (Figures 9 and 10). Since the compliances of fluid-filled inclusions are related to their elongated shapes and their sizes, this leads to the anisotropic characteristics of seismic velocity dispersion and attenuation depicted in Figure 9.

Based on the visualizations of the prevailing energy dissipation process in Figures 10 and 11, our results confirm the observation of Agersborg et al. (2009) that FB-FPD is responsible for the seismic attenuation in carbonate rocks. The characteristic frequency of this manifestation is mainly controlled by the permeability of the embedding porous medium and is expected to be influenced by the geometry and distribution of mesoscopic voids. Due to the preferential orientation of the inclusions, our results show no significant evidence of FPD within the limited number of connected voids. For mesopore networks that are more complex in terms of orientation and interconnectivity, the results might, however, differ in this regard. In the future, we will extend the numerical scheme to the 3D case and will explore the response of more realistic mesopore and/or fracture networks. It should also be noted that seismic attenuation in real carbonate rocks is a multiscale problem. In this work, we focused on mesoscopic FPD effects and, hence, ignored scattering effects and other dissipation mechanisms prevailing at high frequencies, such as attenuation due to macroscopic global flow and microscopic squirt flow.

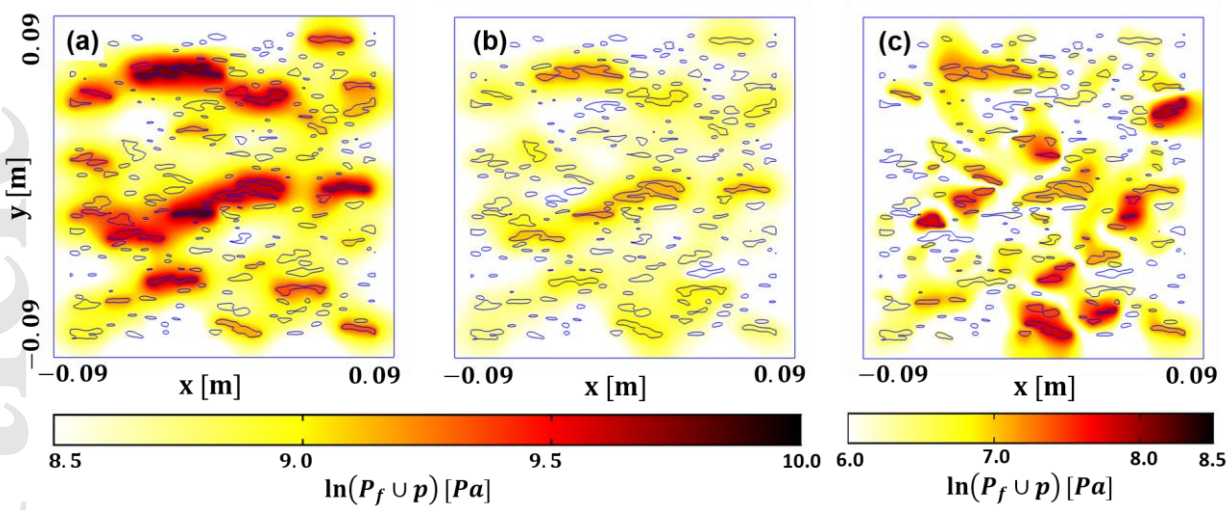

Figure 11. Distribution of fluid pressure at the frequency of the attenuation peak (Figure 9) in the poroelastic background and in the mesoscale voids for *qP*-wave propagation in the (a) vertical direction and (b) horizontal direction. (c) Corresponding results for *qS*-wave propagation in the vertical direction.

4 Discussion

While the numerical results demonstrate the robustness and flexibility of the proposed numerical upscaling procedure to calculate seismic attenuation of porous rocks containing mesoscopic fluid inclusions, assumptions upon which the proposed approach is based merit some consideration. First, we consider that seismic attenuation is controlled by FPD at the mesoscopic scale, and other factors that potentially affect the seismic response at higher frequencies, such as squirt flow (e. g., Gueguen & Sarout, 2011), Biot's global flow and scattering, are neglected. This is reasonable in the seismic exploration frequency band for the considered characteristic sizes of the inclusions. We also assumed that the mesoscopic voids and the embedding porous background are fully saturated with a unique fluid. The partially saturated case warrants further exploration, as the presence of a second fluid phase may change the characteristics of the FPD processes (Solazzi et al, 2021). Moreover, we considered open-pore interface conditions between the fluid inclusions and embedding porous background. Future work should further explore the influence of sealed-pore and partially open-pore interface conditions. In addition, we assumed that there is no slip at

the interface in the tangential direction between the fluid inclusions and porous background. This is reasonable in the framework of small deformation assumed throughout this work.

There are also some intrinsic limitations in the proposed approach. For example, the overall procedure is conceived for heterogeneities having sizes at the mesoscopic scale range and, hence, not appropriate for assessing physical processes occurring at the microscopic scale. In addition, poroelasticity belongs to the macroscopic framework of continuum mechanics (Fortin & Guéguen, 2021), whereas the Navier-Stokes equation determines the behavior of fluids at microscopic scale. In this work, we attempted to couple these two different systems using appropriate interface conditions. To achieve this, at the interface, the microscopic details should be neglected due to the employment of Biot's equations. For the region governed by the Navier-Stokes equation, once the microscopic details of the interface are neglected, the microscopic characteristics of the fluid can be upscaled to the macroscopic and mesoscopic scales (Zampogna et al., 2019). This, in turn, allows the coupling between the fluid region and the adjacent poroelastic system. In this context, it is important to remark that the coupling between a porous medium and a fluid is very common and has wide applications in many fields, such as, for example, geophysics (e. g., Lefeuve-Mesgouez et al., 2012), fluid mechanics (e. g., Badia et al., 2009) and civil engineering (e. g., Vuong et al., 2015). The good agreement of the numerical results obtained using different upscaling approaches supports the correctness of our methodology.

5 Conclusions

We introduced a novel fluid-poroelastic model and an associate numerical upscaling procedure to the determine the effective seismic characteristics of porous rocks containing mesoscopic fluid-filled voids. The model couples the quasi-static NS equations describing the fluid-filled heterogeneities and Biot's consolidation equations for the poroelastic background through appropriate interface conditions. Numerical upscaling is performed through three numerical oscillatory relaxation tests on representative 2D samples characterized by the proposed hybrid fluid-poroelastic model. The averaged stress and strain inferred from the three tests can be used to compute the complex-valued and frequency-dependent stiffness matrix of an effective viscoelastic

medium, which then enables us to calculate the equivalent seismic attenuation and phase velocity spectra. In this context, we also introduce the inverse quality factor density to explore the prevailing attenuation mechanisms in more detail.

We first compare the proposed approach to the purely poroelastic approach as well as the coupled fluid-elastic approach based on a well-known benchmark-type fracture model. We observed that the proposed approach and purely poroelastic approach provide similar results of inverse quality factors and phase velocities provided that the material properties are optimized when representing voids as poroelastic features. Accounting for the effects of asperities along the fracture walls reveals that the two approaches provide consistent results with regard to seismic attenuation due to FB-FPD. Conversely, the results related to FF-FPD significantly differ in terms of the characteristic frequencies associated with the corresponding attenuation peaks, while the magnitudes are comparable. This frequency shift is related to the estimation of the effective permeability of the fracture, which is a key parameter for the purely poroelastic approach. Conversely, the permeability is naturally accounted for through the model geometry in the proposed coupled fluid-poroelastic approach. We also observe that the proposed approach and the coupled fluid-elastic approach predict similar seismic attenuation due to FF-FPD, which further supports the correctness of the proposed approach. However, the limitation of the coupled fluid-elastic approach is that it assumes a fully elastic background and, hence, does not account for FB-FPD. Finally, we explore the seismic characteristics of a synthetic vuggy carbonate-type rock sample using the proposed approach. We observe significant velocity dispersion and attenuation of *qP*- and *qS*-waves in the seismic frequency band, which, based on the spatial distributions of the inverse quality factor density and the fluid pressure, can be attributed to fluid pressure communication between the mesoscopic vugs and microscopic pores of the embedding background.

Appendix A. Analysis of the New Approximation of Effective Strain for Poroelastic Media

In section 2.2, in the framework of the proposed procedure of numerical upscaling, it is necessary to compute the averaged strains over the sample. Since the interpretation is made in a viscoelastic

context, the final values of averaged strain should be consistent with those obtained using the imposed BCs for our problem. In the following, we analyze this consistency for the new approximation of effective poroelastic strains proposed in equation (28). To this end, we consider two oscillatory relaxation tests as illustrated in Figure A1 for the coupled problem, where a fluid inclusion Ω_f is embedded in the porous background Ω_p.

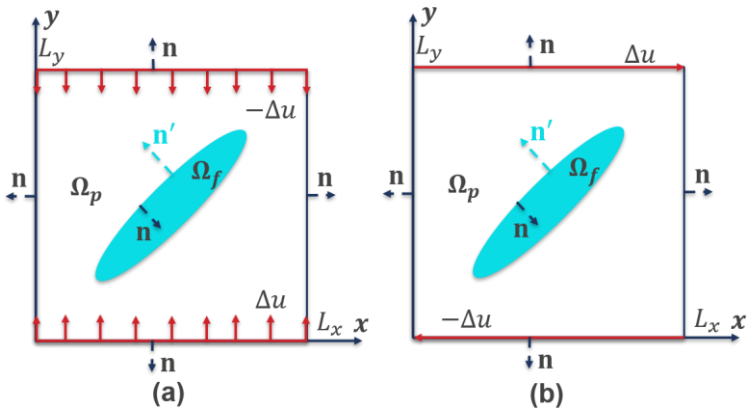

Figure A1. Sketch of 2D coupled fluid-poroelastic problem to analyze the volume average of (a) diagonal components and (b) non-diagonal component of strain.

1. Diagonal components of averaged strain

For the analysis of the diagonal components of averaged strain, we consider the vertical compressibility relaxation test shown in Figure A1(a). We calculate the volume average of the vertical component of strain over the coupled medium as

$$\langle \epsilon_{22} \rangle = \frac{1}{L_x L_y} \int_0^{L_y} \int_0^{L_x} \epsilon_{22}(x,y)\, dx dy = \frac{1}{L_x L_y} \left[\int_{\Omega_p} \varepsilon_{22}^{pm}(x,y)\, dV + \int_{\Omega_f} E_{22}^{f}(x,y)\, dV \right]. \tag{A1}$$

For the poroelastic medium, we consider the new approximation of effective strain proposed in equation (28), for which the vertical component takes the form

$$\varepsilon_{22}^{pm}(x,y) = \frac{\partial (u_2 + w_2)}{\partial y}, \tag{A2}$$

where u_i is the ith component of solid displacement, and w_i is the ith component of fluid displacement relative to the solid matrix. For the fluid inclusion, the vertical component of strain is given by equation (8) as

$$E_{22}^{f}(x,y)=\frac{\partial u_2^f}{\partial y}, \tag{A3}$$

where u_i^f is the *i*th component of fluid displacement.

For mathematical simplicity, we define two functions as

$$\mathbf{P}(x,y)=(0,u_2(x,y)+w_2(x,y)), \qquad \mathbf{Q}(x,y)=\left(0,u_2^f(x,y)\right). \tag{A4}$$

Thus, we have

$$\int_{\Omega_p}\varepsilon_{22}^{pm}(x,y)dV=\int_{\Omega_p}\boldsymbol{\nabla}\cdot\mathbf{P}(x,y)dV\,, \qquad \int_{\Omega_f}E_{22}^{f}(x,y)dV=\int_{\Omega_f}\boldsymbol{\nabla}\cdot\mathbf{Q}(x,y)dV. \tag{A5}$$

By applying the divergence theorem, we get

$$\int_{\Omega_p}\varepsilon_{22}^{pm}(x,y)dV=\int_{\Gamma_p}\mathbf{P}(x,y)\cdot\mathbf{n}ds\,, \qquad \int_{\Omega_f}E_{22}^{f}(x,y)dV=\int_{\Gamma_{pf}}\mathbf{Q}(x,y)\cdot\mathbf{n}'ds\,. \tag{A6}$$

where $\mathbf{n}$ is the outward-directed unit normal vector on the boundaries Γ_p of the porous domain, and Γ_{pf} is a closed trajectory defining the interface of the fluid and porous domains. Note that at the interface, we have $\mathbf{n}=-\mathbf{n}'$.

Operating with equation (A6), we obtain

$$\begin{aligned}\int_{\Omega_p}\varepsilon_{22}^{pm}(x,y)dV=&\int_0^{L_x}\mathbf{P}(x,0)\cdot(0,-1)dx+\int_0^{L_y}\mathbf{P}(L_x,y)\cdot(1,0)dy+\int_0^{L_x}\mathbf{P}\left(x,L_y\right)\cdot(0,1)dx\\&+\int_0^{L_y}\mathbf{P}(0,y)\cdot(-1,0)dy+\int_{\Gamma_{pf}}\mathbf{P}(x,y)\cdot\mathbf{n}ds\,.\end{aligned} \tag{A7}$$

From equation (A4), we have

$$\mathbf{P}(L_x,y)\cdot(1,0)=[0,u_2(L_x,y)+w_2(L_x,y)]\cdot(1,0)=0, \tag{A8}$$

$$\mathbf{P}(0,y)\cdot(-1,0)=[0,u_2(0,y)+w_2(0,y)]\cdot(-1,0)=0. \tag{A9}$$

Considering the imposed BCs on the bottom edge of the REV (equations (14) and (17)), that is, $u_2(x,0)=\Delta u$ and $w_2(x,0)=0$, we have

$$\int_0^{L_x}\mathbf{P}(x,0)\cdot(0,-1)dx=-\Delta u\cdot L_x. \tag{A10}$$

On the top edge of the REV, we impose $u_2\left(x,L_y\right)=-\Delta u$ and $w_2\left(x,L_y\right)=0$ (equations (14) and (17)), so we have

$$\int_0^{L_x} \mathbf{P}(x, L_y) \cdot (0,1) dx = -\Delta u \cdot L_x. \tag{A11}$$

Substituting equations (A8) to (A11) into equation (A7), we get

$$\int_{\Omega_p} \varepsilon_{22}^{pm}(x,y) dV = -2\Delta u \cdot L_x + \int_{\Gamma_{pf}} \mathbf{P}(x,y) \cdot \mathbf{n} ds\,. \tag{A12}$$

For equation (A6), we also have

$$\int_{\Omega_f} E_{22}^{f}(x,y) dV = \int_{\Gamma_{pf}} \mathbf{Q}(x,y) \cdot \mathbf{n}' ds = -\int_{\Gamma_{pf}} \mathbf{Q}(x,y) \cdot \mathbf{n} ds\,. \tag{A13}$$

Substituting equations (A12) and (A13) into equation (A1) yields

$$\langle \epsilon_{22} \rangle = \frac{-2\Delta u}{L_y} + \frac{1}{L_x L_y} \int_{\Gamma_{pf}} [\mathbf{P}(x,y) - \mathbf{Q}(x,y)] \cdot \mathbf{n} ds\,. \tag{A14}$$

Recalling the interface conditions (equations (10) and (11)), we have $\mathbf{u} + \mathbf{w} = \mathbf{u}^f$ at all points of Γ_{pf}, which means that

$$\frac{1}{L_x L_y} \int_{\Gamma_{pf}} [\mathbf{P}(x,y) - \mathbf{Q}(x,y)] \cdot \mathbf{n} ds = 0. \tag{A15}$$

The volume average of strain is finally obtained as

$$\langle \epsilon_{22} \rangle = \frac{-2\Delta u}{L_y}, \tag{A16}$$

which is consistent with the value that we obtain from the imposed BCs.

It is important to remark here that, if the Biot's definition of solid strain is used, we can define the function

$$\mathbf{P}'(x,y) = (0, u_2). \tag{A17}$$

Following a similar derivation, the volume average of strain is obtained

$$\langle \epsilon_{22} \rangle = \frac{-2\Delta u}{L_y} + \frac{1}{L_x L_y} \int_{\Gamma_{pf}} [\mathbf{P}'(x,y) - \mathbf{Q}(x,y)] \cdot \mathbf{n} ds\,. \tag{A18}$$

The second term on the right-hand side of the equation corresponds to a residual due to the incorrect representation of the displacement field of the porous region using a single-phase medium in a viscoelastic context.

We can draw similar conclusions for $\langle \epsilon_{11} \rangle$ if a horizontal compressibility relaxation test is considered, which is omitted here for brevity.

2. Non-diagonal components of averaged strain

For the analysis of the non-diagonal components of strain, we consider the shear relaxation test illustrated in Figure A1(b). The volume average of the shear strain over the REV can be computed as

$$\langle \epsilon_{12} \rangle = \frac{1}{L_x L_y} \int_0^{L_y} \int_0^{L_x} \epsilon_{12}(x,y) dx dy = \frac{1}{L_x L_y} \left[\int_{\Omega_p} \varepsilon_{12}^{pm}(x,y) dV + \int_{\Omega_f} E_{12}^{f}(x,y) dV \right], \tag{A19}$$

where we consider the new approximation of strain $\varepsilon_{12}^{pm}(x,y)$ defined in equation (28) for the poroelastic medium. Thus, we have

$$\int_{\Omega_p} \varepsilon_{12}^{pm}(x,y) dV = \frac{1}{2} \int_{\Omega_p} \left[\frac{\partial (u_1 + w_1)}{\partial y} + \frac{\partial (u_2 + w_2)}{\partial x} \right] dV \,, \tag{A20}$$

and using the definition in equation (8) for the fluid inclusion, we get

$$\int_{\Omega_f} E_{12}^{f}(x,y) dV = \frac{1}{2} \int_{\Omega_f} \left[\frac{\partial u_1^f}{\partial y} + \frac{\partial u_2^f}{\partial x} \right] dV \,. \tag{A21}$$

We define the following functions

$$\mathbf{F}(x,y) = (u_2 + w_2, u_1 + w_1), \quad \mathbf{G}(x,y) = \left(u_2^f, u_1^f\right). \tag{A22}$$

Combining equations (A19) to (A22) and using the divergence theorem, we have

$$\langle \epsilon_{12} \rangle = \frac{1}{L_x L_y} \left[\frac{1}{2} \int_{\Gamma_p} \mathbf{F}(x,y) \cdot \mathbf{n} ds + \frac{1}{2} \int_{\Gamma_{pf}} \mathbf{G}(x,y) \cdot \mathbf{n}' ds \right]. \tag{A23}$$

For the first term on the right-hand side of equation (A23), we have

$$\begin{aligned} \frac{1}{2} \int_{\Gamma_p} \mathbf{F} \cdot \mathbf{n} ds = {} & \frac{1}{2} \int_0^{L_x} \mathbf{F}(x,0) \cdot (0,-1) dx + \frac{1}{2} \int_0^{L_y} \mathbf{F}(L_x,y) \cdot (1,0) dy + \frac{1}{2} \int_0^{L_x} \mathbf{F}\left(x,L_y\right) \cdot (0,1) dx \\ & + \frac{1}{2} \int_0^{L_y} \mathbf{F}(0,y) \cdot (-1,0) dy + \frac{1}{2} \int_{\Gamma_{pf}} \mathbf{F}(x,y) \cdot \mathbf{n} ds \,. \end{aligned} \tag{A24}$$

Considering the imposed BCs on the bottom edge of the REV (equations (22) and (25)), that is, $u_1(x,0) = -\Delta u$ and $w_1(x,0) = 0$, we get

$$\frac{1}{2}\int_0^{L_x}\mathbf{F}(x,0)\cdot(0,-1)dx=\frac{1}{2}\Delta u\cdot L_x. \tag{A25}$$

For the BCs on the right edge of the REV (equations (23) and (25)), we impose $u_2(L_x,y)=0$ and $w_2(L_x,y)=0$. We obtain

$$\frac{1}{2}\int_0^{L_y}\mathbf{F}(L_x,y)\cdot(1,0)dy=0. \tag{A26}$$

On the top edge of the REV (equations (22) and (25)), we impose $u_1\left(x,L_y\right)=\Delta u$ and $w_1\left(x,L_y\right)=0$. We thus have

$$\frac{1}{2}\int_0^{L_x}\mathbf{F}\left(x,L_y\right)\cdot(0,1)dx=\frac{1}{2}\Delta u\cdot L_x. \tag{A27}$$

Finally, on the left edge of the REV (equations (23) and (25)), we impose $u_2(0,y)=0$ and $w_2(0,y)=0$. Thus, we have

$$\frac{1}{2}\int_0^{L_y}\mathbf{F}(0,y)\cdot(-1,0)dy=0. \tag{A28}$$

Substituting equations (A25) to (A28) into equation (A24), we get

$$\frac{1}{2}\int_{\Gamma_p}\mathbf{F}\cdot\mathbf{n}ds=\Delta u\cdot L_x+\frac{1}{2}\int_{\Gamma_{pf}}\mathbf{F}(x,y)\cdot\mathbf{n}ds\,. \tag{A29}$$

For the second term on the right-hand side of the equation (A23), we have

$$\frac{1}{2}\int_{\Gamma_{pf}}\mathbf{G}(x,y)\cdot\mathbf{n}'ds=-\frac{1}{2}\int_{\Gamma_{pf}}\mathbf{G}(x,y)\cdot\mathbf{n}ds. \tag{A30}$$

Substituting equations (A29) and (A30) into equation (A23), we have

$$\langle\epsilon_{12}\rangle=\frac{1}{L_y}\Delta u+\frac{1}{2L_xL_y}\int_{\Gamma_{pf}}[\mathbf{F}(x,y)-\mathbf{G}(x,y)]\cdot\mathbf{n}ds\,. \tag{A31}$$

Recalling the interface condition in equations (10) and (11), we have $\mathbf{u}+\mathbf{w}=\mathbf{u}^f$ at all points of Γ_{pf}, which means that

$$\frac{1}{2L_xL_y}\int_{\Gamma_{pf}}[\mathbf{F}(x,y)-\mathbf{G}(x,y)]\cdot\mathbf{n}ds=0. \tag{A34}$$

Finally, we get

$$\langle \epsilon_{12} \rangle = \frac{\Delta u}{L_y}, \tag{A35}$$

which is the same value as that obtained using the imposed displacement on the outer boundaries.

If the Biot's definition of solid strain is used instead, we define

$$\mathbf{F}'(x, y) = (u_2, u_1). \tag{A36}$$

Following similar steps as before, we obtain

$$\langle \epsilon_{12} \rangle = \frac{\Delta u}{L_y} + \frac{1}{2L_x L_y} \int_{\Gamma_{pf}} [\mathbf{F}'(x, y) - \mathbf{G}(x, y)] \cdot \mathbf{n} ds\,, \tag{A37}$$

where, on the right-hand side of the equation, the integral term is the residual due to an incorrect representation of the displacement field of the porous region using a single-phase medium in a viscoelastic context.

Appendix B. Consistency of the New Approximation of Average Strain with the Energy-based Approach

We consider the same model as presented in Figure 2, and calculate the inverse quality factor of the *qP*-wave for a vertical direction of propagation. We compare the results obtained using the proposed approach based on the dynamic-equivalent viscoelastic assumption with a reference solution obtained using the energy-based approach (equation (38)). More specifically, when using the former, we consider both Biot's definition of solid strain (defined in equation (3)) and the new approximation of strain (equation (28)) for the porous domain to compute the volume average strain of the sample. Results for the proposed coupled fluid-poroelastic approach are depicted in Figure B1(a). We see that the attenuation spectrum corresponding to the new approximation of effective strain is in good agreement with that using the energy-based approach. However, when Biot's definition of solid strain is considered, the attenuation is different from that of the energy-based approach due to the incorrect estimation of the volume average strain of the sample. We also show the results based on the purely poroelastic approach in Figure B1(b). In this case, we observe that both the new approximation and Biot's definition of strain provide the same result as that using the energy-based approach. This agreement is due to the periodicity imposed on the fluid flow at opposite boundaries of the REV. Similar results were also observed for the *qS*-wave, which are omitted here for brevity.

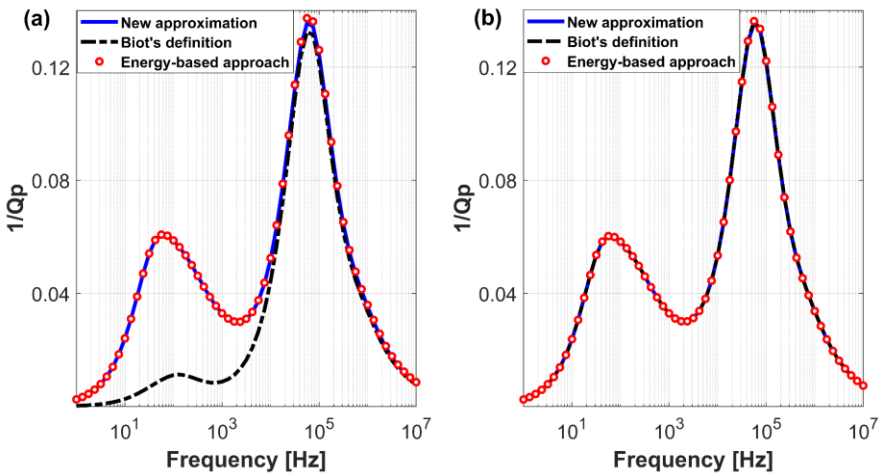

Figure B1. Inverse quality factor of the *qP*-wave as a function of frequency for vertical propagation obtained using (a) the proposed coupled fluid-poroelastic approach and (b) the purely poroelastic approach. The results correspond to the model in Figure 2. For the inputs of the approach based on the dynamic-equivalent viscoelastic assumption, "New approximation" refers to the estimation of average strain in the poroelastic domain using equation (28), while "Biot's definition" denotes using the Biot's definition of solid strain defined in equation (3).

Data Availability Statement

Data sets are available online (https://doi.org/10.5281/zenodo.5574304).

Acknowledgments

J. G. R. gratefully acknowledges the financial support received from the Agencia Nacional de Promoción Científica y Tecnológica of Argentina (PICT 2017-2976). The contributions of N. D. B., M. F., and K. H. benefited from Swiss National Science Foundation grants 196037, 180112, and 178946, respectively. This project has received funding from the European Union's HORIZON 2020 research and innovation programme under the Marie Sktodowska-Curie grant agreement No. 101007851. The work was also supported in part by the National Natural Science Foundation of China (51675402), the National Key R&D Program of China (2018YFC0603501, 2020YFA0713403, and 2020YFA0713400), and the Chinese Scholarship Council (202006280416). We would like to thank the editor Yves Bernabe, the reviewer Yves Guéguen and an anonymous reviewer for their helpful suggestions.

References

Agada, S., Geiger, S., & Doster, F. (2016), Wettability, hysteresis and fracture–matrix interaction during CO2 EOR and storage in fractured carbonate reservoirs. *Int. J. Greenh. Gas Con.*, 46, 57-75.

Ager, C., Schott, B., Winter, M., & Wall, W. A. (2019a), A Nitsche-based cut finite element method for the coupling of incompressible fluid flow with poroelasticity. *Comput. Methods Appl. Mech. Eng.*, 351, 253-280.

Ager, C., Schott, B., Vuong, A. T., Popp, A., & Wall, W. A. (2019b), A consistent approach for fluid-structure-contact interaction based on a porous flow model for rough surface contact. *Int. J. Numer. Methods Eng.*, 119, 1345-1378.

Agersborg, R., Johansen, T. A., & Jakobsen, M. (2009), Velocity variations in carbonate rocks due to dual porosity and wave- induced fluid flow. *Geophys. Prospect.*, 57, 81–98.

Anselmetti, F. S., Luthi, S., & Eberli, G. P. (1998), Quantitative characterization of carbonate pore systems by digital image analysis. *AAPG Bull.*, 82, 1815–1836.

Ba, J., Carcione, J. M., & Nie, J. X. (2011), Biot-Rayleigh theory of wave propagation in double-porosity media. *J. Geophys. Res.*, 116, B06202.

Bailly, C., Fortin, J., Adelinet, M., & Hamon, Y. (2019), Upscaling of elastic properties in carbonates: A modeling approach based on a multiscale geophysical data set. *J. Geophys. Res.*, 124. 13,021–13,038.

Badia, S., Quaini, A., & Quarteroni, A. (2009), Coupling Biot and Navier–Stokes equations for modelling fluid–poroelastic media interaction. *J. Comput. Phys.*, 228(21), 7986-8014.

Barbosa, N. D., Hunziker, J., Lissa, S., Saenger, E. H., & Lupi, M. (2019), Fracture unclogging: a numerical study of seismically induced viscous shear stresses in fluid-saturated fractured rocks. *J. Geophys. Res. Solid Earth*, 124(11), 705-727.

Beavers, G. S., & Joseph, D. D. (1967), Boundary conditions at a naturally permeable wall, *J. Fluid Mech.*, 30, 197–207.

Biot, M. A. (1941), General theory of three- dimensional consolidation. *J. Appl. Phys.*, 12, 155–164.

Biot, M. A. (1962), Mechanics of deformation and acoustic propagation in porous media. *J. Appl. Phys.*, 33, 1482–1498.

Bourbié, T., Coussy, O., & Zinszner, B. (1987), Acoustics of Porous Media, Institut français du pétrole publications.

Ba, J., Carcione, J. M., & Nie, J. (2011), Biot-Rayleigh theory of wave propagation in double-porosity media, *J. Geophys. Res.*, 116, B06202.

Brajanovski, M., Gurevich, B., & Schoenberg, M. (2005), A model for P-wave attenuation and dispersion in a porous medium permeated by aligned fractures. *Geophys. J. Int.*, 163, 372-384.

Burchette, T. P. (2012), Carbonate rocks and petroleum reservoirs: a geological perspective from the industry. Geol. Soc. Lond., Spec. Publ., 370(1), 17-37.

Carcione, J. M., Santos, J. E., & Picotti, S. (2011), Anisotropic poroelasticity and wave-induced fluid flow: harmonic finite-element simulations. *Geophys. J. Int.*, 186, 1245-1254.

Chapman, M. (2003), Frequency-dependent anisotropy due to meso-scale fractures in the presence of equant porosity. *Geophys. Prospect.*, 51, 369–379.

David, E. C., & Zimmerman, R. W. (2011), Elastic moduli of solids containing spheroidal pores. *Int. J. Eng. Sci.*, 49(7), 544–560.

Deresiewicz, H., & Skalak, R. (1963), On uniqueness in dynamic poroelasticity. *Bull. Seismol. Soc. Am.*, 53, 783–788.

Dutta, N. C., & Odé, H. (1979a), Attenuation and dispersion of compressional waves in fluid- filled porous rocks with partial gas saturation (White model), Part I: Results. *Geophysics*, 44, 1777–1788.

Dutta, N. C., & Odé, H. (1979b), Attenuation and dispersion of compressional waves in fluid- filled porous rocks with partial gas saturation (White model), Part II: Results. *Geophysics*, 44, 1789–1805.

Fortin, J. & Guéguen, Y. (2021), Porous and cracked rocks elasticity: Macroscopic poroelasticity and effective media theory. *Math. Mech. Solids*, 1-15.

Gassmann, F., (1951), Über die elastizität poröser medien: vierteljahrsschrift der naturforschenden gesellschaft in Zürich, 96, 1–23.

Goldscheider, N., Chen, Z., Auler, A. S., Bakalowicz, M., & Broda, S., et al. (2020), Global distribution of carbonate rocks and karst water resources. *Hydrogeol. J.*, 28(5), 1-17.

Guéguen, Y. & Sarout, J. (2011), Characteristics of anisotropy and dispersion in cracked medium. *Tectonophysics*, 503, 165-172.

Gurevich, B., & Schoenberg, M. (1999), Interface conditions for biot's equations of poroelasticity. *J. Acoust. Soc. Am.*, 105(5), 2585-2589.

Hudson, J. A. (1981), Wave speeds and attenuation of elastic waves in material containing cracks, *Geophys. J. Int.*, 64, 133–150.

Hunziker, J., Favino, M., Caspari, E., Quintal, B., Rubino, J. G., Krause, R., & Holliger, K. (2018), Seismic attenuation and stiffness modulus dispersion in porous rocks containing stochastic fracture networks. *J. Geophys. Res. Solid Earth*, 123, 125–143.

Jaeger, J. C., Cook, N. G. W., & Zimmerman, R. W. (2007), Fundamentals of rock mechanics. Blackwell.

Jha, M. K., Chowdhury, A., Chowdary, V. M., & Peiffer, S. (2007), Groundwater management and development by integrated remote sensing and geographic information systems: prospects and constraints. *Water. Resour. Manag.*, 21(2), 427-467.

Jian, S. K., Fu, L. Y., Cao, C. H., Han, T. C., & Du, Q. Z. (2021), 3D finite-element modeling of effective elastic properties for fracture density and multiscale natural fractures. *J. Geophys. Eng.*, 4.

Klimentos, T. (1995), Attenuation of P- and S-waves as a method of distinguishing gas and condensate from oil and water. *Geophysics*, 60(2), 447–458.

Landau, L. D., & Lifshitz, E. M. (1959), Fluid mechanics. Pergamon Press.

Lefeuve-Mesgouez, G., Mesgouez, A., Chiavassa, G., & Lombard, B. (2012), Semi-analytical and numerical methods for computing transient waves in 2d acoustic/poroelastic stratified media. *Wave Motion*, 49(7), 667-680.

Lissa, S., Barbosa, N. D., Caspari, E., Alkhimenkov, Y., & Quintal, B. (2020), Squirt flow in cracks with rough walls. *J. Geophys. Res. Solid Earth*, 125, e2019JB019235.

Lissa, S., Barbosa, N. D., Rubino, J. G., & Quintal, B. (2019), Seismic attenuation and dispersion in poroelastic media with fractures of variable aperture distributions. *Solid Earth*, 10, 1321–1336.

Liu, E., Chapman, M., Varela, I., Li, X., Queen, J. H., & Lynn, H., (2007), Velocity and attenuation anisotropy: Implication of seismic fracture characterizations. *The Leading Edge*, 26, 1170-1174.

Liu, E., & Martinez, A. (2012), Seismic fracture characterization: Concepts and practical applications. Houten: European Association of Geoscientists and Engineers.

Masson, Y. J., & Pride, S. R. (2007), Poroelastic finite difference modeling of seismic attenuation and dispersion due to mesoscopic-scale heterogeneity. *J. Geophys. Res*., 112, B03204.

Masson, Y. J., & Pride, S. R. (2014), On the correlation between material structure and seismic attenuation anisotropy in porous media. *J. Geophys. Res. Solid Earth*, 119, 2848-2870.

Mavko, G., Mukerji, T., & Dvorkin, J. (2009), The rock physics handbook: Tools for seismic analysis of porous media. Cambridge: Cambridge University Press.

Montemagno, C., & Pyrak-Nolte, L. J. (1995), Porosity of natural fracture networks, *Geophys. Res. Lett.*, 22, 1397–1400.

Müller, T. M., Gurevich, B., & Lebedev, M. (2010), Seismic wave attenuation and dispersion resulting from wave-induced flow in porous rocks—A review. *Geophysics*, 75, 75A147–75A164.

Pride, S. R., Berryman, J. G., & Harris, J. M. (2004), Seismic attenuation due to wave-induced flow. *J. Geophys. Res.*, 109, B01201.

Quintal, B., Caspari, E., Holliger, K., & Steeb, H. (2019), Numerically quantifying energy loss caused by squirt flow. *Geophys. Prospect.*, 67(8), 2196–2212.

Quintal, B., Rubino, J. G., Caspari, E., & Holliger, K. (2016), A simple hydromechanical approach for simulating squirt-type flow. *Geophysics*, 81(4), D335–D344.

Quintal, B., Steeb, H. Frehner, M., & Schmalholz, S. M. (2011), Quasi- static finite element modeling of seismic attenuation and dispersion due to wave- induced fluid flow in poroelastic media. *J. Geophys. Res.*, 116, B01201.

Rubino, J. G., Caspari, E., Müller, T. M., Milani, M., Barbosa, N. D., & Holliger, K. (2016), Numerical upscaling in 2-D heterogeneous poroelastic rocks: Anisotropic attenuation and dispersion of seismic waves. *J. Geophys. Res. Solid Earth*, 121, 6698–6721.

Rubino, J. G, Caspari, E., Müller, T. M., & Holliger, K. (2017), Fracture connectivity can reduce the velocity anisotropy of seismic waves. *Geophys. J. Int.*, (1), 210, 223-227.

Rubino, J. G., Guarracino, L., Müller, T. M., & Holliger, K. (2013), Do seismic waves sense fracture connectivity?. *Geophys. Res. Lett.*, 40, 692-696.

Rubino, J. G., Müller, T. M., Guarracino, L., Milani, M., & Holliger, K. (2014), Seismoacoustic signatures of fracture connectivity. *J. Geophys. Res.*, 119, 2252– 2271.

Rubino, J. G., M Müller, T. M., Milani, M., & Holliger, K. (2015), Seismic attenuation and velocity dispersion in fractured rocks: The role played by fracture contact areas. *Geophys. Prospect.*, 62(6), 1278-1296.

Rubino, J. G., Ravazzoli, C. L., & Santos, J. E. (2009), Equivalent viscoelastic solids for heterogeneous fluid-saturated porous rocks, *Geophysics*, 74, N1-N13.

Schijns, H., Schmitt, D. R., Heikkinen, P. J., & Kukkonen, I. T. (2012), Seismic anisotropy in the crystalline upper crust: observations and modelling from the Outokumpu scientific borehole, Finland. *Geophys. J. Int.*, 189, 541-553.

Sharma M. D. (2009), Boundary conditions for porous solids saturated with viscous fluid. *Appl. Math. Mech.*, 30, 821–832.

Solazzi, S. G., Hunziker, J., Caspari, E., Rubino, J. G., Favino, M., & Holliger, K. (2020), Seismic signatures of fractured porous rocks: The partially saturated case. *J. Geophys. Res. Solid Earth*, 125(8), e2020JB019960.

Solazzi, S. G., Rubino, J. G., Müller, T. M., Milani, M., Guarracino, L., & Holliger, K. (2016), An energy-based approach to estimate seismic attenuation due to wave- induced fluid flow in heterogeneous poroelastic media. *Geophys. J. Int.*, 207(2), 823–832.

Solazzi, S. G., Lissa, S., Rubino, J. G., & Holliger, K. (2021), Squirt flow in partially saturated cracks: a simple analytical model. *Geophys. J. Int.*, 227(1), 680-692.

Tester, J. W., Anderson, B. J., Batchelor, A. S., Blackwell, D. D., DiPippo, R., Drake, E. M., et al. (2007), Impact of enhanced geothermal systems on US energy supply in the twenty-first century. *Philos. Phil. Trans. R. Soc.*, 365(1853), 1057–1094.

Vinci, C., Renner, J., & Steeb, H. (2014a), A hybrid-dimensional approach for an efficient numerical modeling of the hydro-mechanics of fractures. *Water Resour. Res.*, 50, 1616–1635.

Vinci, C., Renner, J., & Steeb, H. (2014b), On attenuation of seismic waves associated with flow in fractures. *Geophys. Res. Lett.*, 41, 7515–7523.

Vuong, A. T., Yoshihara, L., & Wall, W. A. (2015), A general approach for modeling interacting flow through porous media under finite deformations. *Comput. Methods Appl. Mech. Eng.*, 283, 1240-1259.

Wenzlau, F., Altmann, J. B., & Müller, T. M. (2010), Anisotropic dispersion and attenuation due to wave-induced fluid flow: Quasi-static finite element modeling in poroelastic solids. *J. Geophys. Res.*, 115, B07204.

White, J. E. (1975), Computed seismic speeds and attenuation in rocks with partial gas saturation. *Geophysics*, 40, 224–232.

Zampogna, G. A., Lacis, U., Bagheri, S., & Bottaro, A. (2019), Modeling waves in fluids flowing over and through poroelastic media. *Int. J. Multiphase Flow*, 110, 148-164.